

Formation and Transformation Trends of Metal Carbonates With Cation Ratio and Ion Interaction in Post-treatment Process of Desalination Brine

Injun Kim

Yonsei University <https://orcid.org/0000-0001-9520-0715>

Jinwon Park

Yonsei University

Yunsung Yoo (✉ yysrxn@yonsei.ac.kr)

Yonsei University <https://orcid.org/0000-0003-0321-6950>

Research

Keywords: Carbon capture utilization, CO₂ conversion, Desalination brine post treatment, Metal carbonation

Posted Date: September 21st, 2021

DOI: <https://doi.org/10.21203/rs.3.rs-885713/v1>

License:  This work is licensed under a Creative Commons Attribution 4.0 International License.

[Read Full License](#)

Formation and transformation trends of metal carbonates with cation ratio and ion interaction in post-treatment process of desalination brine

Injun Kim, Jinwon Park[†], Yunsung Yoo[†]

Department of Chemical and Biomolecular Engineering, Yonsei University, Seoul, Republic of Korea

[†]Corresponding author's information

1) Corresponding author: Yunsung Yoo

E-mail: yysrxn@yonsei.ac.kr

Tel: +82-10-5634-6377

2) Corresponding author: Jinwon Park

E-mail: jwpark@yonsei.ac.kr

Tel: +82-2-2123-7430

Abstract

Background

To address the negative effects of desalination plants, CO₂ emissions, and discharge of desalination brine, we studied the carbon capture utilization (CCU) process based on metal carbonation via the reuse of desalination brine. In this study, we converted CO₂ and simulated desalination brine into metal carbonate using monoethanolamine as an aqueous absorbent. The produced metal carbonate varied according to the cation component of the simulated desalination brine. We focused on ion interactions in the aqueous system, occurred by cation ratio, and other phenomena caused by the interactions.

Results

We determined that the common ion effect, which occurred owing to the ion interactions of the system, was the main reason for the various carbonation trends. Ionic atmospheres that were changed by the ionic components significantly affected the trends. The high salinity of the desalination brine also affected the metal carbonation. We further deduced that the variation in the results was derived from interactions between the abovementioned effects. And we also found that Na⁺, which was overlooked in former studies about polymorph transformation, also affects polymorph transformation.

Conclusions

All the phenomena in the metal carbonation interrupt desalination brine post-treatment because of their unpredictability. However, we suggest ambient estimation of its cation components, which would help future studies and demonstrate desalination brine post-treatment.

Keywords : Carbon capture utilization, CO₂ conversion, Desalination brine post treatment, Metal carbonation

1. Background

Desalination process plays a significant role in supplying water worldwide. It is known that 100 billion liters of water are provided via the desalination process, which is consumed for various purposes, such as drinking, agriculture, and industrial fields [1]. For example, Middle Eastern countries such as Saudi Arabia provide 50% of its total water demand via desalination processes, which is becoming increasingly popular as the population grows [2]. Although the desalination process is essential for the survival of human beings, it can cause severe environmental problems. According to Yazan's study, discharged brine and carbon dioxide emissions are major environmental problems that result from the desalination process and significantly affect the ecosystem [3, 4]. Therefore, the desalination process needs to be improved from the viewpoint of sustainable development. Applying carbon capture utilization (CCU) technology to desalination plants will be a key solution to the problems associated with the desalination process.

CCU technology converts CO₂ captured by various methods, such as absorption, adsorption, or separation via membranes, into useful chemical compounds via chemical treatments [5]. Converted CO₂, which is the final product of the CCU process, can be used as a raw material in various industrial fields. Unlike carbon capture storage (CCS) technology, which stores captured CO₂ in underground storage or seabed strata, CCU technology does not require storage space, which means that CCU technology does not have the risk of CO₂ leakage owing to earthquakes or earth surface fluctuations. Furthermore, CCU technology can secure economic benefits by trading the final product of the technology, which can be used in many industrial fields [5-7]. Owing to these advantages, CCU technology is considered a novel solution to global warming, as well as a practical alternative to CCS technology [6-8].

Mineral carbonation-based inorganic CCU is a subcategory of CCU technology that converts CO₂ into inorganic chemical compounds, usually metal carbonates such as CaCO₃ or MgCO₃, by using cations from natural resources or industrial wastes [7, 9]. Mineral carbonation-based inorganic CCU technology can treat large quantities of CO₂ in a short time, and the converted CO₂ can be permanently fixed in the form of mineral carbonates [9, 10]. Furthermore, aqueous absorbents such as monoethanolamine (MEA,

HOCH₂CH₂NH₂) are used to capture CO₂ gas. In this case, CO₂ can be easily converted into mineral carbonates under ambient temperature and pressure conditions as captured CO₂ exists in the ionic phase [11, 12]. Mineral carbonation-based inorganic CCU can be applied to currently operating plants by installing separate post-facilities. In addition, the technical development level of this technology is relatively mature in comparison with other CCU technologies, such as organic CCU, and thus it can be applied to industrial fields in a short time [11, 13].

Many researchers have investigated mineral carbonation-based inorganic CCU characteristics and are seeking to improve the desalination process. To solve the aforementioned problems of desalination plants, many scientists are trying to apply inorganic mineral carbonation CCU to desalination plants [14, 15]. The main idea of these studies is to fix the captured CO₂ gas from a desalination plant by using desalination brine in the form of metal carbonates. Using the proposed technology, the CO₂ emissions and cation concentration of desalination brine can be significant. A conceptual schematic diagram of this process is shown in Fig. 1.

However, previous studies are not suitable for practical applications because of the low quality of the final product and its inconsistent characteristics [11, 13, 16]. These drawbacks of the final product are derived from the complex reaction chemistry of carbonation in multi-cation systems. Because the reaction chemistry in multi-cation systems has not been studied in detail, factors and phenomena that can affect carbonate reactions have not been clearly established. A few studies on controlling the final product characteristics have been presented; however, they focus on precipitation in a single cation system [17, 18], which is far from being industry-applicable because practical processes require ternary cations or more complex cation systems. To overcome the limitations of previous studies, we investigated the precipitation trends and changes in the properties of the final product caused by cation-component variation and ion interactions in a multi-cation system. Carbonation in a multi-cation system follows a competitive reaction because cations mostly react with CO₂ in the system [13, 16, 18]. The number of CO₂ molecules in the system is limited, involving competitive reactions among cations [13]. Hence, it can be hypothesized that the reaction trends are significantly affected by the cation

components of the system, resulting in changes to the properties of the final product.

To understand the correlation between the cation components and precipitation variance, we conducted experiments with simulated desalination brine samples comprising Ca^{2+} , Mg^{2+} , and Na^+ , the representative cation components of desalination brine, to produce metal carbonate in a multi-cation system. Simulated desalination brine is categorized into three types according to the cation components: unary, binary, or ternary cation systems. By categorizing the samples and comparing the results of each type to the others, the impact of cation components on carbonation can be clarified.

We simulated various desalination brine samples using chemical reagents and mixing them with a CO_2 -saturated aqueous absorbent and a 30 wt.% MEA aqueous solution. The cations in the simulated desalination brine were precipitated after mixing with the CO_2 -saturated MEA solution. The properties of the precipitates, including the crystal phase change of the precipitate and metal carbonation preference among cations, were investigated via the following techniques: inductively coupled plasma optical emission spectroscopy (ICP-OES) to determine the cation components and concentrations; X-ray diffraction (XRD) to identify the phases in the precipitate; field emission scanning electron microscopy (FE-SEM) to observe the precipitate morphologies; and energy-dispersive X-ray spectroscopy (EDS) to investigate the atomic components of the precipitate. We analyzed the final products of the experiment using these instruments, both qualitatively and quantitatively.

2. Materials and method

2.1 Materials

All materials used in this study were purchased from Sigma-Aldrich. To capture CO_2 in the simulated flue gases, 400 mL of MEA (purity $\geq 99\%$, CAS No. 141-43-5) in a 30 wt.% aqueous solution was used as the absorbent. Then, we used sodium chloride (purity $\geq 99\%$, CAS No. 7647-14-5), calcium chloride (purity $\geq 99\%$, CAS No. 10043-52-4), and magnesium chloride (purity \geq , CAS No. 7786-30-3) reagents to produce simulated desalination brine containing Ca^{2+} , Mg^{2+} , and Na^+ . We produced 60 simulated desalination brine types, each with a different cation composition.

2.2 Experimental methodology

In this study, two processes, which are CO₂ capture and CO₂ conversion, were considered for the experiments. A 30 wt.% MEA aqueous solution was used as the absorbent to capture CO₂ gas. MEA is the most widely used aqueous absorbent for CO₂ capture in commercial plants [11, 13, 19]. Hence, using MEA can expand the applicability of these research results because commercial mineral carbonation-based inorganic CCU processes are likely to use MEA as an absorbent; thus, the trend of the final industrial product would follow the findings of this study. The molecular structure of amine-based absorbents affects the formation of metal carbonates. Because MEA has a simple molecular structure, it can minimize the effect of molecular structure on mineral carbonation [19]. To investigate the correlation between the cation components and changes in the properties of the final product, i.e., metal carbonate, the effect of the molecular structure can be neglected. Therefore, MEA was considered an appropriate absorbent for this study.

CO₂ conversion experiments were performed using simulated desalination brine. The cations in the simulated desalination brine were designed considering the cation component of desalination brine from various commercial desalination plants [20, 21] and ease of experimentation. The cation concentrations of Na⁺, Mg²⁺, and Ca²⁺ were set at 0.2–0.6 M in 0.2 M increments. As mentioned above, three desalination brine samples were designed (unary, binary, and ternary cation systems) to understand and determine the effect of each cation on the other cation components. These three types of simulated desalination brine were classified in detail according to their cation components: the unary cation system as system Ca⁺ and system Mg²⁺, the binary cation system as system CN (Ca²⁺ and Na⁺), system MN (Mg²⁺ and Na⁺), and system CM (Ca²⁺ and Mg²⁺), and the ternary cation system as system CMN (Ca²⁺, Mg²⁺, and Na⁺). Comparing the experimental results from the various types of desalination brine, using the unary and binary cation systems as the control group and the ternary cation system as the experimental group, could help elucidate the carbonation phenomena in a multi-cation system. The details of the cation composition and molarity of each simulated desalination brine are presented in Table 1. A schematic of the experimental apparatus is illustrated in Fig. 2. A detailed description of the

experiment is provided below.

2.2.1 Experimental setup

Flue gas from coal-fired power plants usually contains 10–20 vol% of CO₂ gas [11, 13, 19]. We modeled the flue gas such that it contained 15 vol% CO₂ and 85 vol% N₂, both of which had high purity (N₂ and CO₂ gas, Sam-Heung Gas, purity > 99.9%). A mass flow controller (MFC, KOFLOC, Japan) was connected to a mass flow indicator (MFI, SEHWA-HIGHTECH, ROK) and used to control the flow rate of the gas passing through the equipment. Using the MFC and MFI, the flows of CO₂ and N₂ were controlled at 300 and 1800 mL/min, respectively. A gas mixer was used to improve the mixing of CO₂ and N₂ gases, and a ceramic gas diffuser made with micro-sized pores (pore size = 0.7 μm) was attached to the end of the air-flow tube. A double-jacket reactor made of Pyrex glass (Pyrex, 300 mL, USA) was connected to a water bath (LC-LT407, LK Lab Korea, ROK) to maintain the temperature of 298.15 K. The experiment was performed at a pressure of 1 atm. During the experiment, the pressure and temperature were maintained at constant values. On the upper side of the reactor, the condenser was connected to a chiller (LC-LT408, LK Lab Korea, ROK) set to 276.15 K. The condenser prevented the aqueous solvent inside the reactor from evaporating, thus avoiding concentration changes owing to heat from the exothermic reaction. A gas analyzer (Gasmaster, sensoronic, ROK) was used to analyze the change in the gas concentration during the absorption experiments. The concentration of the gas from the reactor output was monitored every 30 s, and the results were displayed on a computer screen embedded in the gas analyzer.

2.2.2 Experiment Part 1: CO₂ capture via MEA 30 wt.% solution

A schematic of the experimental apparatus, shown in Fig. 2(a), demonstrates Experiment Part 1, “CO₂ capture via 30 wt.% aqueous MEA solution.”

Before starting the CO₂ absorption experiment, the reactor was purged with high-purity N₂ gas (Sam-Heung gas, purity ≥ 99.99) to remove all impurities. After 5 min of purging, 400 mL of 30 wt.% MEA solution was placed in the double-jacket reactor, and the reactor was sealed with a silicon plug and

vacuum grease. The modeled flue gas, comprising 300 mL/min of CO₂ gas and 1800 mL/min of N₂ gas from the MFC, was fed into the gas mixer. Subsequently, the modeled flue gas flowed into the reactor through the pipe and flowed out through the diffuser. The gas readily mixed with the aqueous absorbent because the diffuser had many small pores, resulting in increased absorption of CO₂ gas. To aid CO₂ absorption, a magnetic bar and an electric stirrer located on the underside of the reactor were used. The stirring rate was set to 300 rpm during the absorption experiments. The gas mixture flowing out of the gas diffuser was allowed to pass through the aqueous solvent. Some of the mixed gas was absorbed in the aqueous absorbent, and the remaining gas was allowed to pass through the condenser for transport to the gas analyzer. During the absorption experiments, the gas analyzer measured the CO₂ gas concentration of the gas mixture flowing out of the reactor. The concentration of CO₂ gas was 0% during the initial stage because most of the gas was rapidly absorbed by the aqueous absorbent. Over time, the concentration of CO₂ that flowed into the gas analyzer increased as the CO₂ absorption capacity of the absorbent decreased. Once the concentration of CO₂ gas displayed on the analyzer screen reached 15%, it was presumed that the 30 wt.% MEA solution was fully saturated with CO₂, and the flow of the mixed gas was stopped, thus completing the CO₂ absorption experiment.

2.1.3. Experiment Part 2: CO₂ conversion via simulated desalination brine

The schematic, shown in Figure 2(b), describes Experimental Part 2, “CO₂ conversion using simulated desalination brine.”

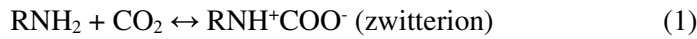
After the CO₂ absorption experiments, a precipitation experiment was conducted, and a precipitate was obtained via mineral carbonation by mixing 200 mL of CO₂-saturated MEA solution (30 wt.%), taken from Experiment Part 1, and 200 mL of the simulated desalination brine (types 1–60). The solutions were mixed at a ratio of 1:1, and 400 mL of the mixture was placed in a beaker equipped with magnetic bars and stirred at 300 rpm at 298.15 K and 1 atm for 90 min. The experimental stirring time was set according to the type of simulated desalination brine to minimize the crystal phase change of the precipitate at equilibrium [19, 22]. After stirring, the mixtures, which produced a white precipitate within a few seconds to a few minutes, were filtered through a fiber filter (Whatman, GF/B) with 1.0-

μm pores. A branched flask connected to a vacuum pump (N-820, KNF, France) was used to separate the precipitate and supernatant. Separated precipitates were dried in a convection oven set to 313.15 K for 24 h and then milled to a powder. After drying, the precipitates were washed with 50 wt.% ethanol solution [13, 23] to remove the residual soluble salt and dried again at a set temperature. The samples were then placed in vials and analyzed by ICP-OES (Perkin Elmer, OPTIMA 8300), XRD (ULTIMA IV, Rigaku, Japan), and FE-SEM (7800F, JEOL, Japan).

3. Results and discussion

3.1 CO₂ absorption and mineral carbonation

We used 200 mL of a 30 wt.% MEA solution for CO₂ absorption. MEA is classified as a primary amine because it has an amine functional group. Equations (1–3) describe the CO₂ absorption phenomenon of the primary or secondary amine [11, 23].



<Total equation>



As described in Eqs. 1–3, 2 mol of MEA reacts with 1 mol of CO₂, and the reacted CO₂ produces carbamate, the ionic phase of CO₂ [11, 19, 23]. The absorbed CO₂ molecules were calculated using this reaction. The molarity of the 30 wt.% MEA solution was 4.91 M, and CO₂ fully saturated the 30 wt.% MEA solution with 2.46 M of saturated CO₂. This calculation was verified based on the experimental data from the gas analyzer, where Eq. 4 was used to calculate the amount of absorbed CO₂ using data from the gas analyzer [13, 16, 19, 23].

$$\dot{N}_{CO_2} = \dot{f}_{CO_2} \times \left(\frac{C_{in} - C_{out}}{C_{in}} \right) \times \Delta\tau \quad (4)$$

\dot{N}_{CO_2} : Number of moles of absorbed CO₂ (mol)

\dot{f}_{CO_2} : CO₂ flow rate into the reactor (mol/s)

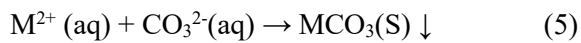
C_{in} : Concentration of CO₂ flowing out of vent (vol%)

C_{out} : Concentration of CO₂ flowing into from reactor (vol%)

$\Delta\tau$: Time interval (s)

Figure 3 shows the CO₂ loading curve of the 30 wt.% MEA solution. The loading value of the 30 wt.% MEA solution is 0.55 mol of CO₂/mol of MEA. The gap between the theoretical loading value and the experimental value is the result of CO₂ absorption by H₂O. Because H₂O also absorbs a small amount of CO₂ gas, the experimental loading value is higher than the theoretical value [11, 23]. Thus, the absorption experiment was verified, and the CO₂ concentration of the saturated absorbent, i.e., 30 wt.% MEA solution, was 2.70 M. Because the maximum concentration of each cation was 0.6 M, it seems that the ionic CO₂ concentration for metal carbonation was sufficient.

As mentioned above, absorbed CO₂ exists as an aqueous phase that easily reacts with metal cations owing to its kinetic characteristics [11, 19, 23]. Hence, the cations in the simulated desalination brine easily reacted with CO₃²⁻ in the saturated absorbents. The reaction between dication (M²⁺) and CO₃²⁻ is mineral carbonation, and the equation of the reaction is shown below [11, 19, 23].



When the simulated desalination brine was mixed with the saturated absorbent, the cation reacted with saturated CO₂, producing a precipitate in a mixture of saturated absorbents and simulated desalination brine. We analyzed the precipitate based on the obtained data, and the details of the analysis are provided in the following section.

3.2 Characteristic of precipitation under system type of simulated desalination brine

As mentioned in Section 2.2, we categorized the simulated desalination brine into three types based on its cation component: unary system (samples 1–6), binary system (samples 7–33), and ternary system (samples 34–60). Based on the obtained data, the change in the precipitation characteristics according to the system type was verified. We analyzed the data using the system types of simulated desalination brine to investigate its precipitation characteristics.

3.2.1 Quantitative analysis methods for characterizing precipitation

In this study, we used four quantitative analysis methods, including recovery yield (R), $[\text{Mg}^{2+}]/[\text{Ca}^{2+}]$ ratio (M), XRD retrieval, and O/dication ratio (h), to investigate the trend of carbonation.

Recovery yield (R) is an index based on the results of ICP-OES analysis. Because the input quantity of cations in each simulated desalination brine sample was known, R was calculated using the following equation:

$$R: \text{Cation recovery yield } \left(\frac{\text{mol}}{\text{mol}}\right) \% = \frac{\text{precipitate weight (g)} \times \text{weight proportion of cation (wt \%)} \times \frac{1}{\text{molar mass } \left(\frac{\text{mol}}{\text{g}}\right)}}{\text{input cation mol (mol)}} \quad (6)$$

The main chemical reaction in the mixture of the CO_2 -saturated absorbent and the simulated desalination brine is metal carbonation between the cation and ionic CO_2 [11, 13, 23]; thus, it is possible to investigate the trend of metal carbonation by calculating the cation recovery yield from each sample.

$[\text{Mg}^{2+}]/[\text{Ca}^{2+}]$, M , is a molar ratio-based index that represents the cation molar composition of metal carbonate or simulated desalination brine. According to previous studies, the $[\text{Mg}^{2+}]/[\text{Ca}^{2+}]$ ratio affects the formation of metal carbonates [22, 24–26]. In a multi-cation system, the ratio of the mother solution determines which metal carbonate is formed. The properties of the produced metal carbonate vary according to the ratio of the precipitate [24, 27]. On that basis, we quantified the dication molar composition and analyzed the changes in metal carbonate crystal properties, including crystal phase, by

M.

Furthermore, we applied the XRD retrieval method to quantify the crystal phase of the precipitate [28, 29]. Via the retrieval, the crystal phase composition of the precipitate was calculated, which helped in the detailed quantitative analysis of the precipitate using the *M* index.

The O/dication ratio (*h*) is an EDS analysis-based index. Because amorphous metal carbonate exists in the hydrate phase ($MCO_3 \cdot nH_2O$), *h* can represent the composition of the amorphous metal carbonate in the precipitate. The *h* index can be used as an auxiliary method for estimating the degree of crystallinity. In this analysis, the resolution of the EDS was 15 kV.

3.2.2 Result of control group experiment

We carried out a control group experiment using unary and binary cation systems to clarify the reasons and driving forces of phenomena related to metal carbonation in the ternary cation system. Because it is well known that Na^+ hardly precipitates as a carbonate because of its solubility [13], Na^+ alone was not considered for the experiments. The experiments carried out for the control group were as follows: unary cation system for system Ca^{2+} and system Mg^{2+} , binary cation system for system CN (Ca^{2+} and Na^+), system [19] MN (Mg^{2+} and Na^+), and system CM (Ca^{2+} and Mg^{2+}).

3.2.2.1 Characteristics of precipitation in unary cation system

In the unary cation system, the recovery yield of both Ca^{2+} and Mg^{2+} increased proportionally with the cation concentration, as shown in Figs. 4(a) and (b). The Ca^{2+} recovery yield, R_{Ca} , was above 92% in all three samples, and it slightly increased with increasing Ca^{2+} concentration of each sample. The Mg^{2+} recovery yield, R_{Mg} , also increased with increasing Mg^{2+} concentration. We suspect that this increase of both Ca^{2+} and Mg^{2+} was derived from the salting-out effect. As the cation concentration increases, the salinity of the system increases, thereby increasing the output of the metal carbonate [19, 30]. R_{Mg} was relatively low compared to R_{Ca} , which resulted from the difference in the energy barrier for carbonation. The activation energy for $CaCO_3$ is $-110.5 \text{ kJ mol}^{-1}$ [31], whereas the activation energy for $MgCO_3$ is

63 kJ mol⁻¹ [32]. Therefore, MgCO₃ formation is difficult and reacts slowly in comparison to CaCO₃, resulting in a lower recovery yield.

Figure 4(c) shows the XRD graph of the precipitate from the Ca²⁺ system. Calcite and vaterite, two polymorphs of CaCO₃, were detected. As the Ca²⁺ concentration of the sample increased, the vaterite peak was predominantly detected in the XRD graph, which was verified by the XRD diffraction values listed in Table 2. In short, the crystal phase of the precipitate showed variation with cation concentration.

The FE-SEM images of the precipitate from samples 1, 2, and 3 also showed the predominance of vaterite with cation concentration, consistent with the XRD analysis. As shown in Figs. 5(a), (b), and (c), all the particles observed in the SEM images of the precipitate exhibited spherical and hexagonal shapes, which are representative of the crystal shapes of vaterite and calcite, respectively. In the samples, the spherical particles were dominant with cation concentration.

The cation concentration involves a change in the ionic strength. Using Debye and Hückel's equation (Eq. 7), the ionic strength was calculated as [19]

$$I = \frac{1}{2} \sum_{i=1}^n c_i z_i^2 \quad (7)$$

I: molar ionic strength

c: concentration of ion

z: charge number of ion

As shown in Eq. 7, the increased cation concentration enhanced the ionic strength in the simulated desalination brine sample. In short, the precipitate produced in the simulated desalination brine with higher ionic strength had more vaterite than the simulated desalination brine with lower ionic strength. Moreover, the XRD and FE-SEM results show that the crystal phase of the precipitate could be changed by changing the ionic strength.

We speculate that the vaterite dominance is owing to the interaction between H₂O molecules and the

CaCO₃ polymorphs, caused by ionic strength changes. Amorphous calcium carbonate (ACC, CaCO₃·*n*H₂O) is formed first in the metal carbonation process. Subsequently, it is dehydrated and transformed into vaterite, followed by dissolution [33, 34]. During the final stage of transformation, it is transformed into calcite, the most stable phase among the polymorphs of CaCO₃ [11, 19, 33]. We propose that the dominance of vaterite indicates that increased ionic strength inhibits dissolution. According to Bogunia's study, increased ionic strength activates the hydrophobic interaction of particles in an aqueous solution [35], and various former studies also support this result [19, 30, 36]. Based on this, we assumed that an increase in ionic strength activated the dehydration of ACC and inhibited vaterite dissolution. This phenomenon resulted in the dominance of vaterite in the precipitate as the ionic strength increased.

The results of the EDS analysis for the precipitate of system Ca²⁺, presented in Table 3, support the assumption of the change in the CaCO₃ polymorph phase. The O/Ca ratio, *h_{Ca}*, of each sample decreased as the Ca²⁺ concentration increased. As mentioned above, *h_{Ca}* represents the composition of the amorphous metal carbonate in the precipitate. A decrease in the *h* index with increasing ionic strength indicates a decrease in hydrated CaCO₃ (CaCO₃·*n*H₂O), AAC, and the composition of the precipitate, which means that increased ionic strength activates hydrophobic characteristics [35].

However, unlike system Ca²⁺, there was no specific change in the magnesium carbonate crystal phase with Mg²⁺ concentration. In the XRD graph of the precipitate from the Mg²⁺ system, shown in Fig. 4(d), only MgCO₃·3H₂O (nesquehonite) was detected in each XRD graph, regardless of its Mg²⁺ concentration. This result is consistent with the FE-SEM results, which are shown in Figs. 5(d)–(f). As shown in the figures, the precipitate particles had an orthorhombic shape, which is identical to nesquehonite [19]. No other shapes were detected in those samples, demonstrating that the precipitate from these samples mainly consisted of nesquehonite. Owing to the strong hydrophilic characteristic of Mg²⁺ [19, 37], MgCO₃ was produced in the hydrated phase as nesquehonite [38]. We believe that this strong hydrophilic characteristic is the main reason for nesquehonite formation regardless of the Mg²⁺ concentration. Because its hydrophilic behavior is too strong to inhibit, H₂O molecules were still bound

with magnesium carbonate molecules, even with enhanced ionic strength, thus activating hydrophobic behavior. As shown in Table 3, there was little difference in the proportion of h_{Mg} with the Mg^{2+} concentration, indicating that the hydration level of $MgCO_3$ in the precipitate is vital regardless of the Mg^{2+} concentration. This result indicates that the hydrophilic characteristic of Mg^{2+} is too strong to be unaffected by the enhanced ionic strength.

3.2.2 Characteristics of precipitation in binary cation system

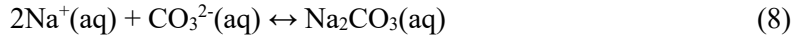
Herein, 27 samples (samples 7–33) of simulated desalination brine containing three types of metal cations, Ca^{2+} , Mg^{2+} , and Na^+ , were used to conduct the conversion experiment. Among these three metal ions, each simulated desalination brine sample contained two types of metal ions, Ca^{2+} and Na^+ (system CN), Mg^{2+} and Na^+ (system MN), and Ca^{2+} and Mg^{2+} (system CM). These three types of control groups showed different precipitation trends based on the cation components of the reaction system. For this reason, we studied the precipitation tendency of binary cation systems by categorizing the systems into two cases as described below.

3.2.2.1 Precipitation in system CN ($Ca^{2+} + Na^+$) and MN ($Mg^{2+} + Na^+$)

The first case is system CN and system MN, where the two types of metal cations that constitute the samples have different valence numbers. Table 4 presents the cation recovery yield and crystal phase composition of the precipitates from the binary cation system. The listed indices, except R , indicate that the precipitation trends of systems CN, MN, and the unary system are very similar, regardless of the presence of Na^+ .

Comparing the R value of unary cation systems with those of binary cation systems CN and MN, we observed that R increased with increasing Ca^{2+} or Mg^{2+} concentration and Na^+ concentration. We speculate that this occurred because of the salting-out effect of Na_2CO_3 [19, 39].

Unlike dication, such as Ca^{2+} and Mg^{2+} , Na^+ produces soluble products such as Na_2CO_3 . Equation 8 describes the chemical reaction for Na^+ production [13].



As described, Na^+ exists in the aqueous phase in the system as Na_2CO_3 . It does not precipitate but rather creates a salting-out effect, causing a moderate boost in the precipitation of CaCO_3 and MgCO_3 [19, 39].

The variance of the crystal phase and its composition of the binary system is similar to that of the unary system. As shown in Figs. 6(c) and (d), vaterite was predominantly detected in system CN with increasing Ca^{2+} concentration, and only nesquehonite was detected in system MN. FE-SEM images of the samples from systems CN and MN also support this result. Figure 7 shows the crystal shape of the precipitate from system CN, and Fig. 8 shows the crystal shape of the precipitate from system MN. As shown, the precipitates are very similar to those of the unary cation system, system Ca^{2+} and system Mg^{2+} , indicating that the results are consistent with the XRD results.

Table 5 lists the EDS analysis results of the precipitates from systems CN and MN. The h_{Ca} value decreased with increasing Ca^{2+} concentration, which is identical to the trend of h_{Ca} in system Ca^{2+} . The h_{Mg} value in the MN system did not depend on Mg^{2+} concentration like the h_{Mg} value in system Mg^{2+} . Furthermore, the Na^+ concentration did not affect either h_{Ca} and h_{Mg} .

Based on ICP-OES, XRD, FE-SEM, and EDS analysis results, we concluded that the dication precipitation tendency in systems CN and MN was not significantly different from that in the unary system. Even Na^+ caused only a slight increase in the dication recovery yield. Most precipitation trends, including crystal phase, XRD diffraction, and h , were very similar to the trends in the unary cation system, indicating that Na^+ ions in the binary cation system did not significantly affect precipitation.

3.2.2.2 Precipitation trends in system CM ($\text{Ca}^{2+} + \text{Mg}^{2+}$)

We investigated the carbonation trend of system CM (samples 25–33), a type of binary cation system. Ca^{2+} and Mg^{2+} , the cation components of system CM, produce insoluble metal carbonates such as CaCO_3 and MgCO_3 , reacting with CO_3^{2-} . The chemical equations for these are as follows [13, 18, 19]:



Because the amount of CO_3^{2-} present in the system is limited, Ca^{2+} conversion into CaCO_3 is a competitive reaction to Mg^{2+} conversion into MgCO_3 and vice versa. If one reaction is dominant, the other is relatively rare, which means that the reaction pathway of each reaction is affected by the other. Because of the competitive nature of this reaction, the cation precipitation trends in system CM were significantly different from those of the unary system [13, 23] and the binary systems CN and MN.

The crystal phase composition of the precipitate from the CM system and R is listed in Table 4. As shown, the phase composition shows indistinct trends with respect to the cation concentration. And we noticed that there was no specific correlation between R and its concentration. To make the trends more noticeable, we display the R of each sample in Figs. 9(a) and (b). Considering the correlation between R and cation concentration in the unary cation system (system Ca^{2+} and system Mg^{2+}) and in the binary systems CN and MN, R should have increased with cation concentration because the system contained sufficient reactants. In short, R_{Ca} and R_{Mg} also showed indistinct correlations with cation concentration, and this trend appeared more strongly in R_{Mg} than in R_{Ca} . Comparing Figs. 9(a) and (b), we noticed that the irregularities of R_{Mg} were higher than those of R_{Ca} . The reason for this phenomenon is shown in Fig. 10, based on the Debye–Hückel theory [40].

According to the Debye–Hückel theory, ions in the electrolyte have an ionic atmosphere that attracts oppositely charged ions and repels similarly charged ions. An increase in the number of ions, which means enhanced ionic strength, cause a widened ionic atmosphere, inhibiting the reaction between cations and anions, which increases the solubility of insoluble salts in electrolytes with enhanced ionic strength and a salting-in effect [40]. In system CM, concentrated dication indicates a double-concentrated anion, and the counter anion is Cl^- . The ionic atmosphere of the double-concentrated anion shields CO_3^{2-} to react with dication, such as Ca^{2+} or Mg^{2+} , causing a decreased dication recovery yield.

Because Ca^{2+} easily reacts with CO_3^{2-} because of its low energy barrier, appropriate ionic radius, and

standard Gibbs free energy for CaCO_3 [11, 13], Cl^- has little effect on the Ca^{2+} recovery yield. However, Mg^{2+} is strongly affected by the increased ionic atmosphere, derived from the concentrated Cl^- ions, because of its small ionic radius, ionic potential causing hydro-shell, and its relatively high energy barrier for carbonation. [31, 32]. As a result, the Mg^{2+} recovery yield was lower than the Ca^{2+} recovery yield in all the system CM samples.

Furthermore, the change in the dication composition of the simulated desalination brine changed the spatial arrangement and distance between the ions in the system. This change affected the interaction between dication and anion and the coordination number [38, 41], resulting in a recovery yield change for each cation, as shown in Figs. 9(a) and (b).

Figure 9(c) shows the XRD graphs of the precipitate samples belonging to system CM. The crystal phase detected in the samples was mostly monohydrocalcite ($\text{CaCO}_3 \cdot \text{H}_2\text{O}$), which is a metastable phase of the CaCO_3 polymorph. Monohydrocalcite usually transforms into calcite through dehydration unless a specific Mg^{2+} concentration exists in the system [24, 27, 42]. Furthermore, monohydrocalcite can only be produced when the $[\text{Mg}^{2+}]/[\text{Ca}^{2+}]$ ratio of the mother solution, M_S , is 0.17 or higher and $[\text{CO}_3^{2-}]$ is higher than $[\text{Ca}^{2+}]$ of the mother solution [27]. The detailed conditions and processes for monohydrocalcite formation are shown in Fig. 11 [24, 27, 42, 43].

M value of system CM is listed in table 6. Because the initial cation concentration of all the samples (samples 25–33) met this condition, the results of the XRD analysis for system CM were reasonable except for samples 28 and 31, which showed the absence of active peaks. The results of the two samples indicate that most metal carbonate in the precipitate existed in an amorphous phase under certain conditions. This means that some factors help metal carbonate maintain an amorphous state for a long time.

According to Jensen's study, MgCO_3 in amorphous calcium magnesium carbonate (ACMC) promotes the interaction between CaCO_3 and H_2O , preventing the dehydration of CaCO_3 [44]. ACC and amorphous magnesium carbonate (AMC) exist in the form of $\text{MCO}_3 \cdot n\text{H}_2\text{O}$ [27, 43, 45]. Thus, MgCO_3

in ACCM would have inhibited the dehydration process, preventing ACC transformation, as indicated by the absence of monohydrocalcite in the system. Based on this, we concluded that the molar ratio of the Mg^{2+} content in the system, definitely over $2 M_s$ ($[Mg^{2+}]/[Ca^{2+}]$ ratio in the mother solution), would have promoted significant interactions between H_2O and metal carbonate, inhibiting the formation of monohydrocalcite [44].

Figure 12 shows the FE-SEM images of the precipitate of system CM. We categorized the particle shapes of each sample into two groups: precipitates with a highly structured shape and those with a low-structured shape. As shown Table 6, and Fig. 12, four samples (25, 26, 27, and 30) with M_p values under 0.4 had highly structured shapes and five samples with M_p values over 0.4 had low-structured shapes. This result is consistent with previous studies whose results are shown in Fig. 11. This phenomenon was caused by the interaction between AMC and ACC in clustered ACCMs during the dehydration process of ACC [26, 27, 43, 45].

The EDS results and h_{Di} (O/Ca+Mg) values are listed in Table 5. We found that the h_{Di} values of system CM showed a constant trend with the initial cation concentration of the simulated desalination brine sample: the h_{Di} value increased with increasing M_s . Because a low h_{Di} value indicates a low level of H_2O interaction with the particles that consist of the precipitate, this result suggests that Mg^{2+} accelerates the interaction between the precipitate and H_2O molecules, which is consistent with the results of previous studies [44, 46]. The high Mg content of the precipitate involves inactive interactions between H_2O molecules and precipitates [37, 44, 46]. This result indicates that the EDS results are also consistent with the XRD, ICP-OES, and FE-SEM results.

Based on the research on binary cation systems, we studied changes in precipitation trends with the cation components of system types. The reason for the difference between the system types is the common ion effect. In systems CN and MN, a salting-out effect occurred. However, in system CM, a salting-in effect occurred, resulting in different trends to systems CN and MN. The ion component affects the solution chemistry of the system, and resulting in various changes to the precipitate.

3.2.3 Characteristics of precipitation in ternary cation system

We studied the precipitation tendency of ternary cation systems based on the investigation of unary and binary cation systems. Because of its similarities to desalination brine, precipitation trends occurring in the ternary cation system are thought to be similar to those of desalination brine produced in industrial fields.

3.2.3.1 Cation recovery yield in system CMN

The cation recovery yield and crystal phase composition of the precipitate from system CMN with $[\text{Na}^+] = 0.2 \text{ M}$, 0.4 M , and 0.6 M are listed in Tables 7. R appears to have an independent relationship with cation concentration, as it did in system CM. To make it easy to notice, R with cation concentration is described in Fig.13. Based on the study of the precipitation trend of system CM, we suspect that the independence between concentration and recovery yield is caused by the common ion effect, as shown in Fig.10.

However, comparing the R value of each sample in system CMN with that of each sample in system CM using the same Ca^{2+} and Mg^{2+} concentrations demonstrated differences. For example, samples 33, 42, 51, and 60 had the same Ca^{2+} and Mg^{2+} concentrations, but their dication, Ca^{2+} , and Mg^{2+} recovery yield differed. We considered two factors that may have caused this phenomenon: the common ion effect and coordination number change. As mentioned above, the salting-in effect results in the independence of R with increasing cation concentration. Ca^{2+} - Mg^{2+} interactions in system CMN had a salting-in effect. However, Na^+ in system CMN had a salting-out effect, and thus it affected R . Two opposite phenomena coincided in system CMN, and they led to the difference of R of system CMN with Na^+ concentration compared to R of system CM.

The cation composition of the system changes with Na^+ concentration, causing a change in the coordination number of the dication. For this reason, there is also a difference in R in system CMN with Na^+ concentration.

Because of the independence of R with cation concentration of system CMN caused by the mixed

phenomenon, predicting the R value of each sample based on cation concentration is difficult. However, local estimating is possible via experimental data, which would help related future studies and demonstrate the process.

3.2.3.2 Crystal phase and shape of precipitate categorized in system CMN

Table 8 lists the dication composition and the M value of system CMN with Na^+ concentration, and Fig. 14 shows the XRD graph of the corresponding precipitate. The monohydrocalcite peak was most frequently detected in 22 out of the 27 samples of system CMN. Because the M_S value of the system CMN samples exceeded 0.17, the formation of monohydrocalcite was an expected result, consistent with previous studies.

However, the XRD analysis results indicated that aragonite and magnesium calcite formed in samples 35 and 36, respectively. This result was not consistent with the other samples, including the control group experiment and previous studies. Considering that the M_S values of the two samples were over 0.17, monohydrocalcite should have formed.

According to previous studies, aragonite is formed in Ca^{2+} - and Mg^{2+} -rich solutions, such as seawater [25, 47-49] and in vitro owing to biomineralization [50]. Because the formation conditions for aragonite are similar to those of monohydrocalcite, previous studies could not establish specific differences between the conditions [51, 52]. ACMC transformation into aragonite via monohydrocalcite [51], or directly [52] is controversial, but it is clear that Na^+ inhibited the role of Mg^{2+} in these two samples because Mg^{2+} plays an indispensable role in the formation of monohydrocalcite [26, 27, 43, 45]. This indicates that Na^+ is also involved in the transformation pathway of ACMC.

In samples 26 and 27, the experimental group for samples 35 and 36, monohydrocalcite formed in the Na^+ -free system. However, in samples 35 and 36, categorized in system CMN with $[\text{Na}^+] = 0.2 \text{ M}$, aragonite and magnesian–calcite formed, which means that Mg^{2+} in those two samples did not trigger monohydrocalcite formation. The difference between the control and experimental groups was the Na^+ content in the system. Based on this, we confirmed once again that Na^+ is involved in the transformation

pathway.

However, in samples 26 and 27 (system CMN with $[\text{Na}^+] = 0.4 \text{ M}$) and samples 35 and 37 (system CMN with $[\text{Na}^+] = 0.6 \text{ M}$), monohydrocalcite formed, demonstrating that Mg^{2+} worked properly. This means that only a specific Na^+ content can weaken the effect of Mg^{2+} on the transformation pathway. Therefore, future studies on metal carbonation and polymorph transformation should consider the Mg/Ca content of the system with Na^+ content.

The M_P values of system CMN also appear consistent with previous studies: crystal shape depends on M_P [19, 24, 26, 27, 43]. However, differences appeared in samples where the nesquehonite peak was detected (i.e., samples 42, 49, 50, 51, 58, and 59). As shown in Table 8, these samples have M_P values higher than 0.4, despite exhibiting highly structured monohydrocalcite particles. The FE-SEM images, shown in Figs. 15–17 also demonstrate that monohydrocalcite and nesquehonite formed in these samples. In the images, orthorhombic-shaped particles, which are suspected to be nesquehonite, appear separately from the structured-monohydrocalcite. This indicates that although the samples containing nesquehonite had high M_P values, the Mg content in the clustered particles was not higher than 0.17. AMC in the sample would have transformed into nesquehonite in the system containing a certain amount of Na^+ , causing highly structured monohydrocalcite formation under high M_P values.

In short, highly structured monohydrocalcite formed in the system CMN, even with M_P values of more than 0.4, demonstrating that Na^+ affects the ACMC transformation pathway.

Table 9 lists the EDS results of system CMN with Na^+ concentration. The h_{Di} value does not show specific correlation with cation concentration. In the control group experiment, h_{Di} increases or decreases with cation concentration. However, in system CMN, because of the complex components, various phenomenon affect h_{Di} , resulting in indistinct correlation with its cation component.

4. Conclusion

In this study, we studied trends of mineral carbonation in simulated desalination brine according to the cation components to improve the efficiency and economics of the mineral carbonation-based CCU

process.

We replicated 60 samples of simulated desalination brine with Ca^{2+} , Mg^{2+} , and Na^+ , which are the main components of desalination brine from desalination plants. Each simulated desalination brine had various cation components and concentrations, and they were used in CO_2 conversion experiments with a CO_2 -saturated aqueous absorbent, MEA. The cations in the simulated desalination brine reacted with saturated CO_2 to produce metal carbonate. We analyzed the metal carbonate using ICP-OES, XRD, and SEM, and focused on quantitative and qualitative analysis for carbonation via various indices such as R , M , and h .

Each simulated desalination brine produced a similar final product with its cation components. However, the carbonation trends of each sample, such as recovery yield, XRD diffraction, M value, and h value, differed with the cation concentration. We concluded that the reason for this difference is the common ion effect caused by ions in the simulated desalination brine. Different ion tribes have different types of common ion effects. Na^+ ions cause salting-out effects, and the interaction between Mg^{2+} and Ca^{2+} causes a salting-in effect in the simulated desalination brine. The concentration of each cation changed the strength of the two different common ion effects and thus the carbonation trends in each desalination brine sample.

This study has significant scientific implications as it analyzes the phenomena occurring in multi-cation systems based on solution chemistry, deriving key points that have not been elucidated in previous studies. Through this study, we expect that effective treatment of CO_2 emissions and desalination brine, which are major problems in desalination plants, could be possible. Furthermore, this study will contribute to CO_2 emission reduction by using desalination brine, a type of industrial waste.

List of Abbreviations

CCU: carbon capture utilization

CCS: carbon capture storage

MEA: monoethanolamine

MFC: mass flow controller

MFI: mass flow indicator

ACC: amorphous Calcium carbonate

AMC: amorphous magnesium carbonate

ACMC: amorphous calcium magnesium carbonate.

Declarations

Ethics approval and consent to participate

Not applicable.

Consent for publication

Not applicable.

Competing interests

There is no competing or related interest on this research article

Availability of data and materials

All data generated or analysed during this study are included in this published article

Contribution

IJ mainly wrote this article. He designed and carried out the experiments, analyzed the results and interpreted the data.

YS and JW supervised the experiment and verified analysis of the result. YS and JW also reviewed the manuscript before the submission and the article was revised by YS and JW.

Corresponding author

Corresponding to Yunsung Yoo and Jinwon Park

Funding

This work was supported by the KOREA SOUTH-EAST POWER CO. (No. 2020-KOEN(Yeongdong)-02) and the Technology Innovation Program (20005884, Development of Membrane Contactor Having High Specific Surface Area as Sulfur Oxides Scrubber) funded by the Ministry of Trade, Industry and Energy (MOTIE, Korea).

Acknowledgements

The authors would like to acknowledge KOREA SOUTH-EAST POWER CO and MOTIE, Korea for providing funding of the research

References

1. AL-MUTAZ IS (1987) By-product recovery from saudi desalination plants. *Desalination* 64:97-110.
2. Alper E, Yuksel Orhan O (2017) CO₂ utilization: Developments in conversion processes. *Petroleum* 3:109-126. doi:10.1016/j.petlm.2016.11.003
3. Azdarpour A, Asadullah M, Mohammadian E, Hamidi H, Junin R, Karaei MA (2015) A review on carbon dioxide mineral carbonation through pH-swing process. *Chemical Engineering Journal* 279:615-630. doi:10.1016/j.ccej.2015.05.064
4. Blue CR, Giuffre A, Mergelsberg S, Han N, De Yoreo JJ, Dove PM (2017) Chemical and physical controls on the transformation of amorphous calcium carbonate into crystalline CaCO₃ polymorphs. *Geochimica et Cosmochimica Acta* 196:179-196. doi:10.1016/j.gca.2016.09.004
5. Bogunia M, Makowski M (2020) Influence of Ionic Strength on Hydrophobic Interactions in Water: Dependence on Solute Size and Shape. *J Phys Chem B* 124:10326-10336. doi:10.1021/acs.jpcc.0c06399
6. Butterworth-Heinemann (2000) Specialised and advanced water treatment processes
7. Cantaert B, Kuo D, Matsumura S, Nishimura T, Sakamoto T, Kato T (2017) Use of Amorphous Calcium Carbonate for the Design of New Materials. *Chempluschem* 82:107-120. doi:10.1002/cplu.201600457
8. D. Sheila PRK (1989) Precipitation of magnesium carbonate. *Hydrometallurgy* 22:249-258. doi:https://doi.org/10.1016/0304-386X(89)90055-8
9. Debye PH, Erich (1923) The theory of electrolytes. I. Freezing point depression and related phenomena. *Physikalische Zeitschrift* 24:185-206.
10. Di Tommaso D, de Leeuw NH (2010) Structure and dynamics of the hydrated magnesium ion and of the solvated magnesium carbonates: insights from first principles simulations. *Phys Chem Chem Phys* 12:894-901. doi:10.1039/b915329b
11. Dong H, Unluer C, Yang E-H, Al-Tabbaa A (2018) Recovery of reactive MgO from reject brine via the addition of NaOH. *Desalination* 429:88-95. doi:10.1016/j.desal.2017.12.021
12. E.García Calvo MAA, P. Letón, (1990) Effects of impurities in the kinetics of calcite decomposition,. *Thermochimica Acta*, Volume 170,: 7-11. doi:https://doi.org/10.1016/0040-6031(90)80519-5
13. Fattah KP, Al-Tamimi AK, Hamweyah W, Iqbal F (2017) Evaluation of sustainable concrete produced with desalinated reject brine. *International Journal of Sustainable Built Environment* 6:183-190. doi:10.1016/j.ijbsbe.2017.02.004
14. Fukushi K, Matsumiya H (2018) Control of Water Chemistry in Alkaline Lakes: Solubility of Monohydrocalcite and Amorphous Magnesium Carbonate in CaCl₂-MgCl₂-Na₂CO₃Solutions. *ACS Earth and Space Chemistry* 2:735-744. doi:10.1021/acsearthspacechem.8b00046
15. Hajbi F, Hammi H, M'nif A (2010) Reuse of RO Desalination Plant Reject Brine. *Journal of Phase Equilibria and Diffusion* 31:341-347. doi:10.1007/s11669-010-9727-3
16. Hosseini T, Selomulya C, Haque N, Zhang L (2014) Indirect Carbonation of Victorian Brown Coal Fly Ash for CO₂ Sequestration: Multiple-Cycle Leaching-Carbonation and Magnesium Leaching Kinetic Modeling. *Energy & Fuels* 28:6481-6493. doi:10.1021/ef5014314
17. Hosseini T, Selomulya C, Haque N, Zhang L (2015) Investigating the Effect of the Mg²⁺/Ca²⁺ Molar Ratio on the Carbonate Speciation during the Mild Mineral Carbonation Process at Atmospheric Pressure. *Energy & Fuels* 29:7483-7496. doi:10.1021/acs.energyfuels.5b01609
18. Ibrahim Y, Arafat HA, Mezher T, AlMarzooqi F (2018) An integrated framework for sustainability assessment of seawater desalination. *Desalination* 447:1-17. doi:10.1016/j.desal.2018.08.019
19. Ikeda T, Boero M, Terakura K (2007) Hydration properties of magnesium and calcium ions from constrained first principles molecular dynamics. *J Chem Phys* 127:074503. doi:10.1063/1.2768063
20. Jensen ACS, Imberti S, Habraken WJEM, Bertinetti L (2020) Small Ionic Radius Limits Magnesium Water Interaction in Amorphous Calcium/Magnesium Carbonates. *The Journal of Physical Chemistry C* 124:6141-6144. doi:10.1021/acs.jpcc.9b11594
21. Jones F, Rohl A, Rickard W, Boon M (2019) Stabilisation of Aragonite: The Role of Mg²⁺ and

- Other Impurity Ions. Chemrxiv. doi:10.26434/chemrxiv.11364857.v1
22. Juma K. Al-Handhaly AMOM, Munjed Maraqa (2003) Impact of chemical composition of reject brine from inland desalination plants on soil and groundwater. *Desalination* 156:89. doi:https://doi.org/10.1016/S0011-9164(03)00330-8
 23. Kang D, Lee M-G, Jo H, Yoo Y, Lee S-Y, Park J (2017) Carbon capture and utilization using industrial wastewater under ambient conditions. *Chemical Engineering Journal* 308:1073-1080. doi:10.1016/j.cej.2016.09.120
 24. Kang D, Park S, Jo H, Park J (2014) Carbon fixation using calcium oxide by an aqueous approach at moderate conditions. *Chemical Engineering Journal* 248:200-207. doi:10.1016/j.cej.2014.03.045
 25. Kang D, Yoo Y, Park J, Lee MG (2018) Chemical conversion of carbon dioxide via target metal separation using seawater-derived wastewater. *ChemistrySelect* 3:8628-8636. doi:10.1002/slct.201702960
 26. Kawano J, Sakuma H, Nagai T (2015) Incorporation of Mg²⁺ in surface Ca²⁺ sites of aragonite: an ab initio study. *Progress in Earth and Planetary Science* 2:7. doi:10.1186/s40645-015-0039-4
 27. Kim I, Yoo Y, Son J, Park J, Huh I-S, Kang D (2019) Two-step mineral carbonation using seawater-based industrial wastewater: an eco-friendly carbon capture, utilization, and storage process. *Journal of Material Cycles and Waste Management* 22:333-347. doi:10.1007/s10163-019-00950-1
 28. Klaus S. Lackner DPB, Christopher H. Wendt (1997) Progress on biding CO₃ in mineral substrates. *Energy Conversion and Management* 38:S259-S264. doi:https://doi.org/10.1016/S0196-8904(96)00279-8
 29. Meylan FD, Moreau V, Erkman S (2015) CO₂ utilization in the perspective of industrial ecology, an overview. *Journal of CO₂ Utilization* 12:101-108. doi:10.1016/j.jcou.2015.05.003
 30. Mezher T, Fath H, Abbas Z, Khaled A (2011) Techno-economic assessment and environmental impacts of desalination technologies. *Desalination* 266:263-273. doi:10.1016/j.desal.2010.08.035
 31. Missimer TM, Maliva RG (2018) Environmental issues in seawater reverse osmosis desalination: Intakes and outfalls. *Desalination* 434:198-215. doi:10.1016/j.desal.2017.07.012
 32. Montes-Hernandez G, Renard F, Auzende A-L, Findling N (2020) Amorphous Calcium–Magnesium Carbonate (ACMC) Accelerates Dolomitization at Room Temperature under Abiotic Conditions. *Crystal Growth & Design* 20:1434-1441. doi:10.1021/acs.cgd.9b01005
 33. Na J, Park S, Bak JH, Kim M, Lee D, Yoo Y, Kim I, Park J, Lee U, Lee JM (2019) Bayesian Inference of Aqueous Mineral Carbonation Kinetics for Carbon Capture and Utilization. *Industrial & Engineering Chemistry Research* 58:8246-8259. doi:10.1021/acs.iecr.9b01062
 34. Nishiyama R, Munemoto T, Fukushi K (2013) Formation condition of monohydrocalcite from CaCl₂–MgCl₂–Na₂CO₃ solutions. *Geochimica et Cosmochimica Acta* 100:217-231. doi:10.1016/j.gca.2012.09.002
 35. Park S, Jo H, Kang D, Park J (2014) A study of CO₂ precipitation method considering an ionic CO₂ and Ca(OH)₂ slurry. *Energy* 75:624-629. doi:10.1016/j.energy.2014.08.036
 36. Pérez-Fortes M, Bocin-Dumitriu A, Tzimas E (2014) CO₂ Utilization Pathways: Techno-Economic Assessment and Market Opportunities. *Energy Procedia* 63:7968-7975. doi:10.1016/j.egypro.2014.11.834
 37. Pham TA, Kweon KE, Samanta A, Lordi V, Pask JE (2017) Solvation and Dynamics of Sodium and Potassium in Ethylene Carbonate from ab Initio Molecular Dynamics Simulations. *The Journal of Physical Chemistry C* 121:21913-21920. doi:10.1021/acs.jpcc.7b06457
 38. Purgstaller B, Konrad F, Dietzel M, Immenhauser A, Mavromatis V (2017) Control of Mg²⁺/Ca²⁺ Activity Ratio on the Formation of Crystalline Carbonate Minerals via an Amorphous Precursor. *Crystal Growth & Design* 17:1069-1078. doi:10.1021/acs.cgd.6b01416
 39. Rodriguez-Blanco JD, Shaw S, Bots P, Roncal-Herrero T, Benning LG (2014) The role of Mg in the crystallization of monohydrocalcite. *Geochimica et Cosmochimica Acta* 127:204-220. doi:10.1016/j.gca.2013.11.034
 40. Ronen Zangi MH, and B. J. Berne (2007) Effect of ions on the hydrophobic interaction between two plates. *Journal of the American Chemical Society* 129:4678-4686. doi:DOI: 10.1021/ja068305m
 41. Sheng K, Ge H, Huang X, Zhang Y, Song Y, Ge F, Zhao Y, Meng X (2020) Formation and Inhibition of Calcium Carbonate Crystals under Cathodic Polarization Conditions. *Crystals* 10.

doi:10.3390/cryst10040275

42. Su J, Zhu F, Zhang G, Wang H, Xie L, Zhang R (2016) Transformation of amorphous calcium carbonate nanoparticles into aragonite controlled by ACCBP. *CrystEngComm* 18:2125-2134. doi:10.1039/c5ce02288f
43. Suryanarayana C, Norton MG (1998) *X-Ray Diffraction*. Springer Science & business Media, New York, USA
44. Walker JM, Marzec B, Nudelman F (2017) Solid-State Transformation of Amorphous Calcium Carbonate to Aragonite Captured by CryoTEM. *Angew Chem Int Ed Engl* 56:11740-11743. doi:10.1002/anie.201703158
45. Xu J, Yan C, Zhang F, Konishi H, Xu H, Teng HH (2013) Testing the cation-hydration effect on the crystallization of Ca-Mg-CO₃ systems. *Proc Natl Acad Sci U S A* 110:17750-17755. doi:10.1073/pnas.1307612110
46. Xu Y, Sommerdijk N (2018) Aragonite formation in confinements: A step toward understanding polymorph control. *Proc Natl Acad Sci U S A* 115:8469-8471. doi:10.1073/pnas.1811696115
47. Yoo Y, Kang D, Choi E, Park J, Huh I-S (2019) Morphology control of magnesium carbonate for CO₂ utilization using Mg²⁺ ions in industrial wastewater depending on length of alkyl chain of primary alkanolamine, reaction temperature, CO₂ concentration, and Mg²⁺/Na⁺ ratio. *Chemical Engineering Journal* 370:237-250. doi:10.1016/j.cej.2019.03.209
48. Yoo Y, Kang D, Kim I, Park J (2018a) Characteristics of Metal Cation Carbonation and Carbon Dioxide Utilization Using Seawater-Based Industrial Wastewater. *ChemistrySelect* 3:9284-9292. doi:10.1002/slct.201800346
49. Yoo Y, Kang D, Kim I, Park J (2018b) Investigation of Thermodynamic Properties on CO₂Absorbents Blended with Ammonia, Amino Acids, and Corrosion Inhibitors at 313.15, 333.15, and 353.15 K. *Journal of Chemical & Engineering Data* 63:2856-2867. doi:10.1021/acs.jced.8b00175
50. Yoo Y, Kang D, Park J (2021) Advanced pseudopolymorph control of magnesium carbonates using structural properties of amines for CO₂ utilization based on post-treatment of desalinated brine. *Desalination* 505. doi:10.1016/j.desal.2020.114904
51. Zhang G, Delgado-López JM, Choquesillo-Lazarte D, García-Ruiz JM (2015) Growth Behavior of Monohydrocalcite (CaCO₃·H₂O) in Silica-Rich Alkaline Solution. *Crystal Growth & Design* 15:564-572. doi:10.1021/cg5010775
52. Zhu F, Nishimura T, Sakamoto T, Tomono H, Nada H, Okumura Y, Kikuchi H, Kato T (2013) Tuning the stability of CaCO₃ crystals with magnesium ions for the formation of aragonite thin films on organic polymer templates. *Chem Asian J* 8:3002-3009. doi:10.1002/asia.201300745

Figures

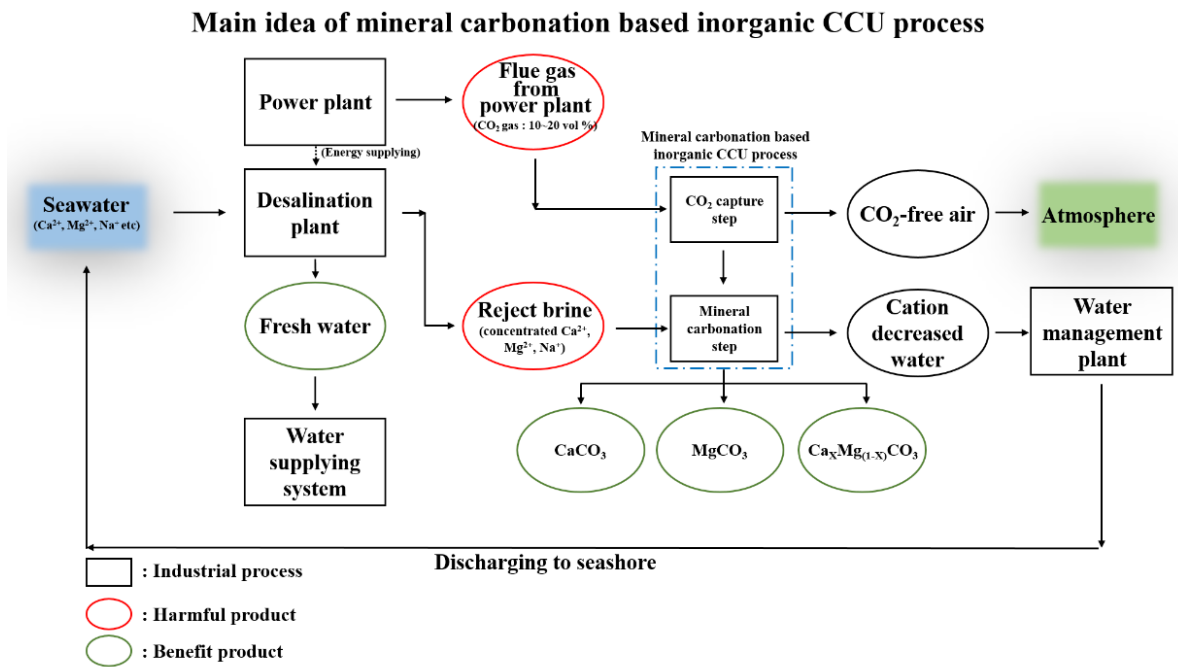


Fig. 1 Conceptual diagram for mineral carbonation-based inorganic CCU process using desalination brine from desalination plant.

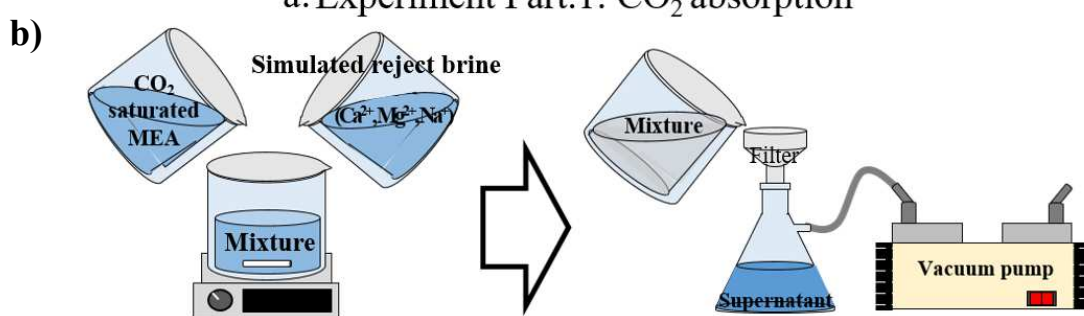
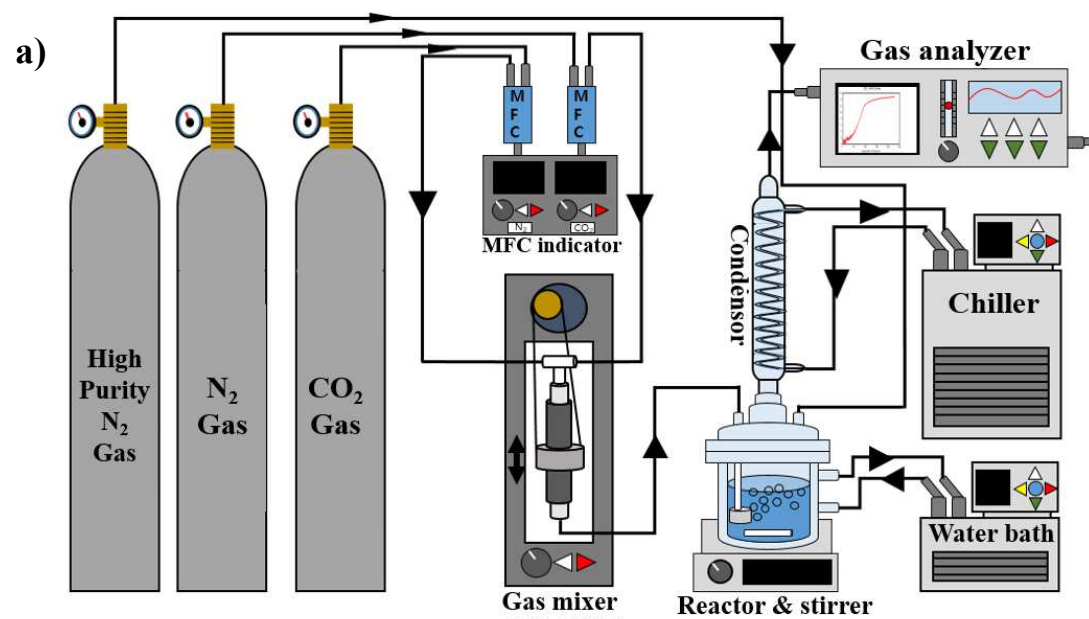


Fig. 2. Schematics of (a) CO₂ absorption and (b) conversion experiment.

Loading curve of 30wt% MEA solution

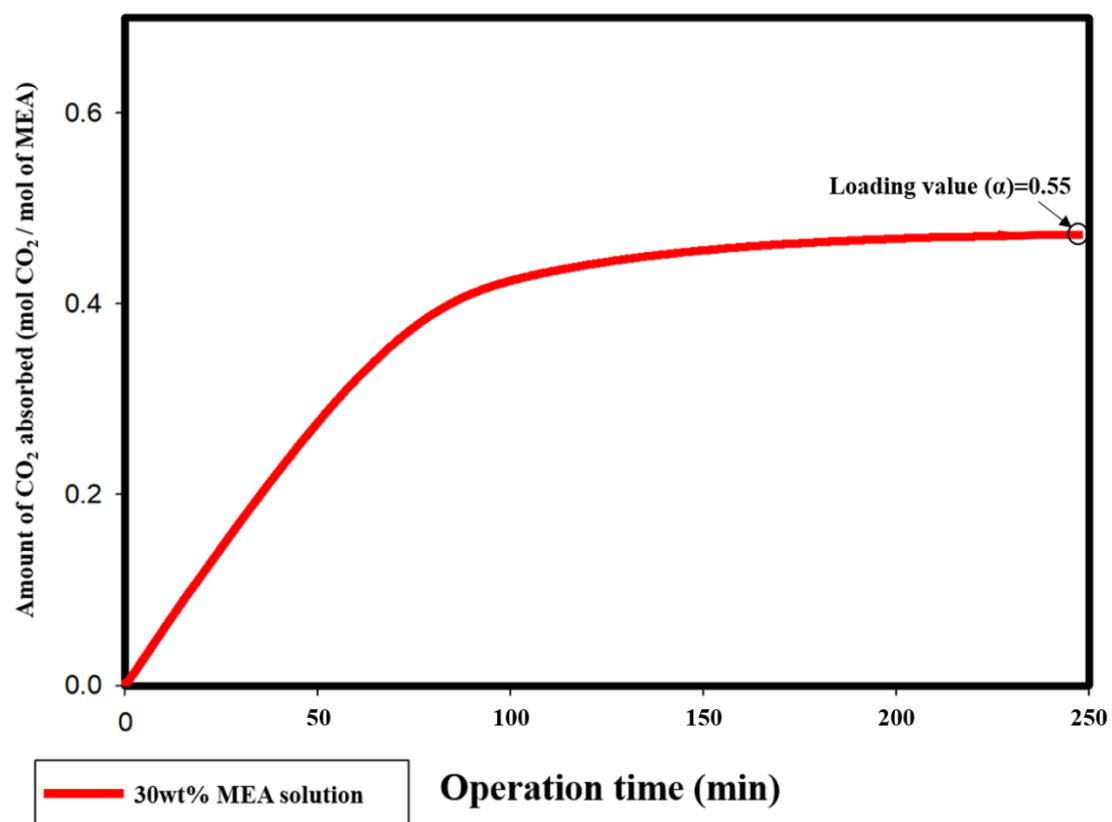


Fig. 3. CO₂ loading curve of the 30 wt.% MEA aqueous solution.

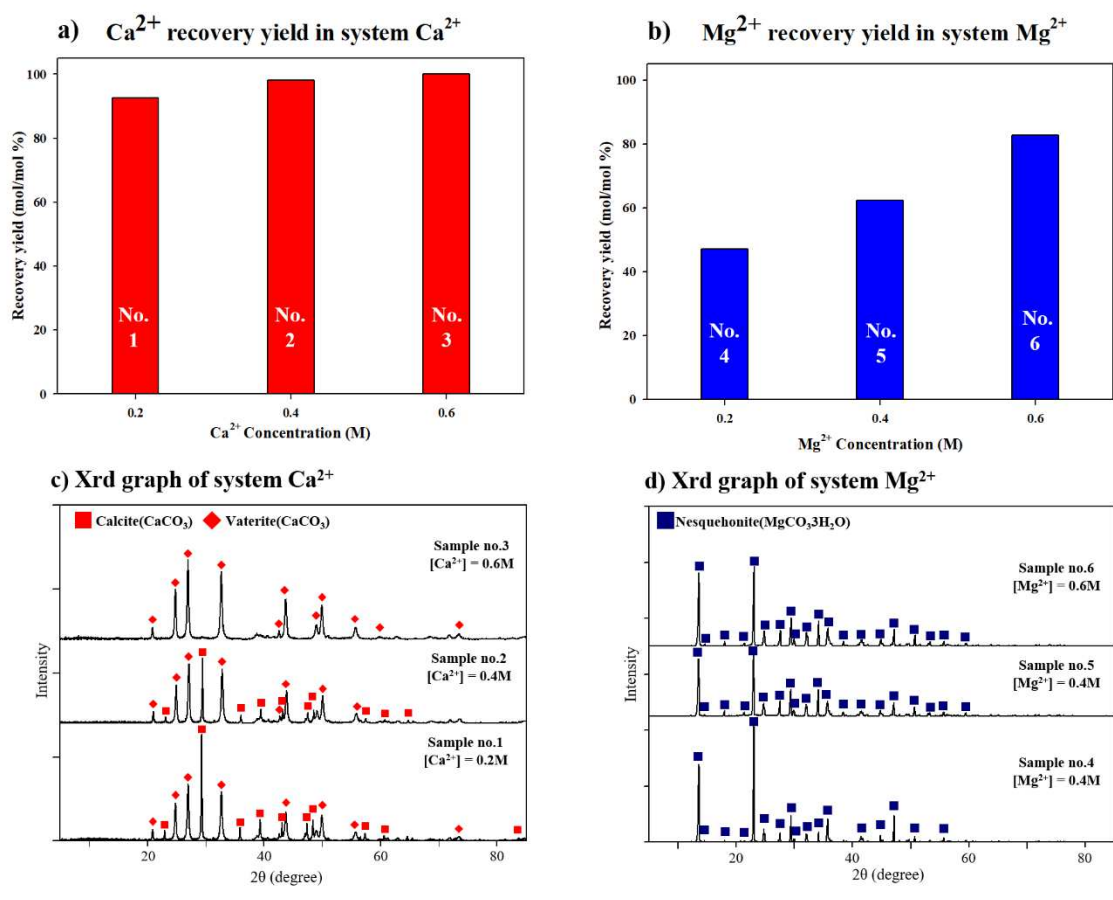


Fig. 4 Cation precipitation trend in unary cation system: (a) Ca^{2+} recovery yield in Ca^{2+} system with Ca^{2+} concentration (number in the bar is sample number) and (b) Mg^{2+} recovery yield in Mg^{2+} system with Mg^{2+} concentration. XRD graphs of precipitate (c) in system Ca^{2+} and (d) system Mg^{2+}

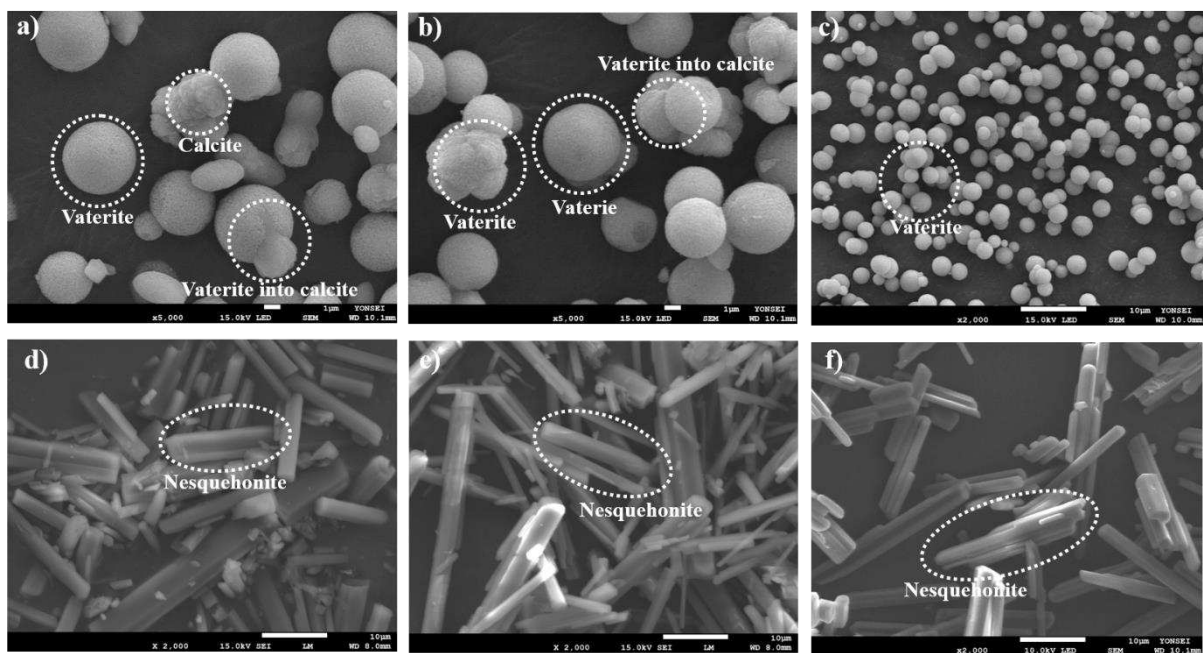


Fig. 5 FE-SEM images of precipitates categorized in unary cation system: (a) from system Ca^{2+} with $[\text{Ca}^{2+}] = 0.2 \text{ M}$ (sample no. 1), (b) from system Ca^{2+} with $[\text{Ca}^{2+}] = 0.4 \text{ M}$ (sample no. 2), (c) from system Ca^{2+} with $[\text{Ca}^{2+}] = 0.6 \text{ M}$ (sample no. 3), (d) from system Mg^{2+} with $[\text{Mg}^{2+}] = 0.2 \text{ M}$ (sample no. 4), (e) from system Mg^{2+} with $[\text{Mg}^{2+}] = 0.4 \text{ M}$ (sample no. 5), and (f) from system Mg^{2+} with $[\text{Mg}^{2+}] = 0.6 \text{ M}$ (sample no. 6)

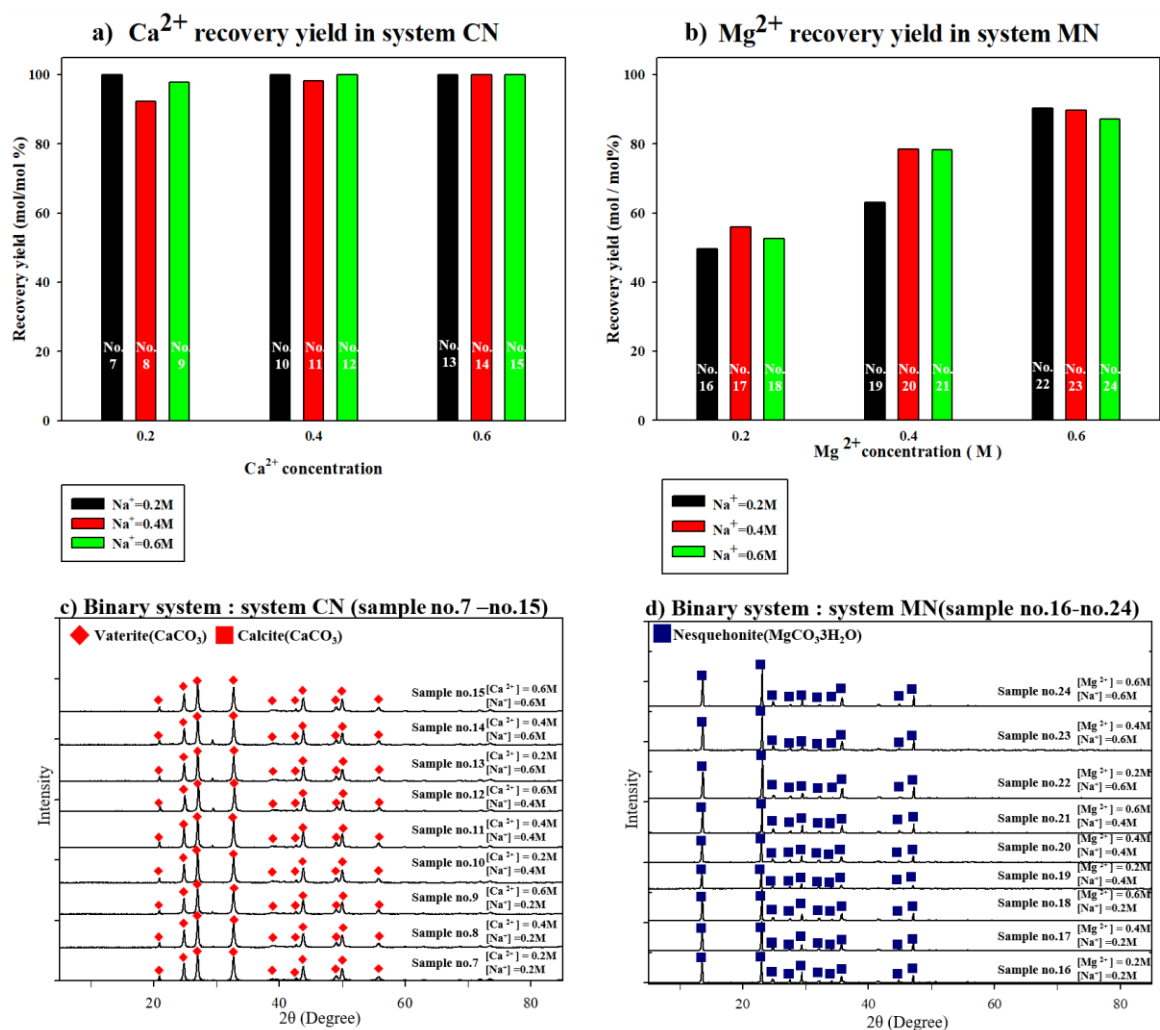


Fig. 6. Cation precipitation trend in binary cation system including system CN and system MN (a) Ca^{2+} recovery yield in system CN with Ca^{2+} and Na^+ concentration (number in the bar is sample number) and (b) Mg^{2+} recovery yield in system MN with Mg^{2+} and Na^+ concentration. XRD graphs of precipitate (c) in system CN and (d) system MN.

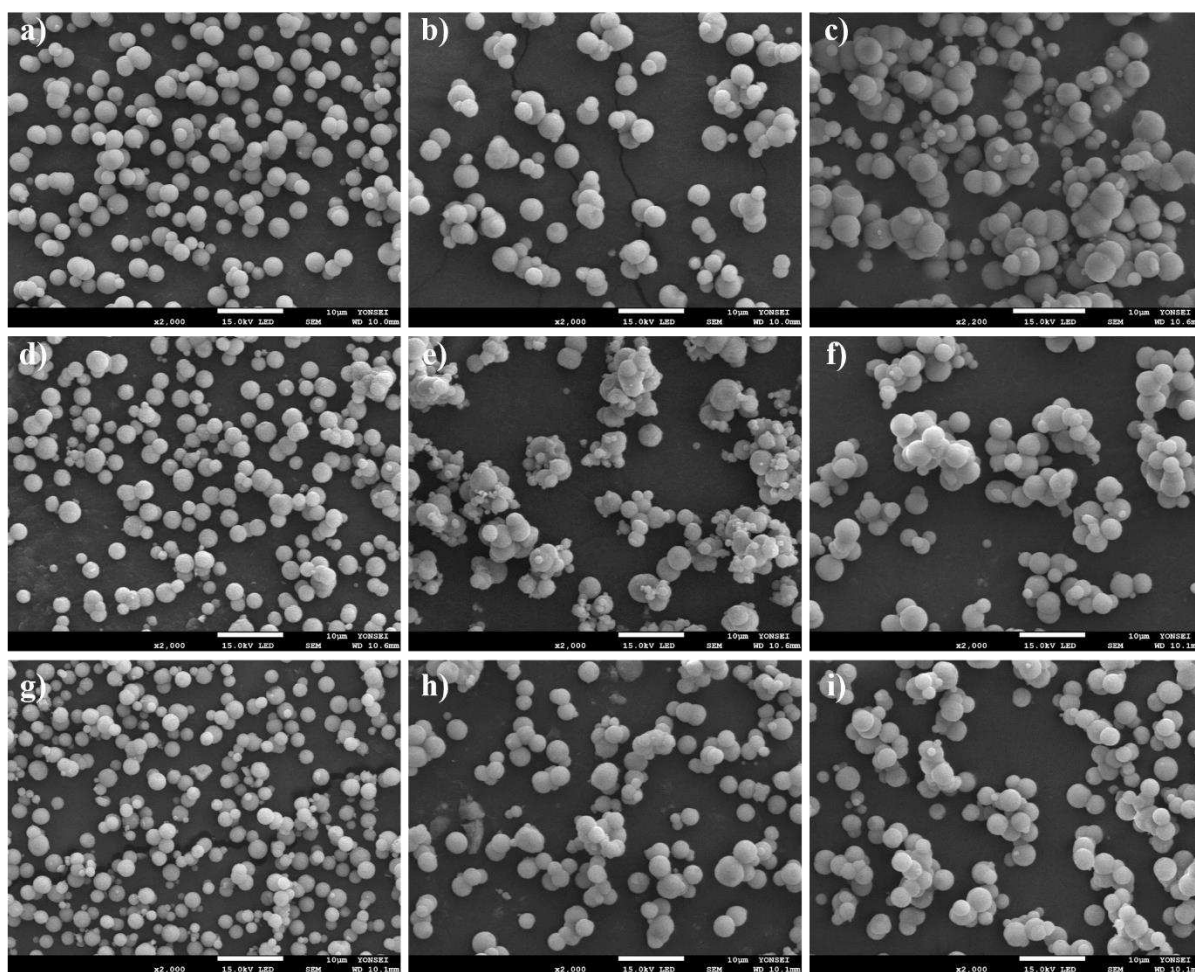


Fig. 7. FE-SEM images of precipitates from system CN. Each images shows crystal shape of precipitate in each sample according to Ca^{2+} and Na^+ concentration. (a) $[\text{Ca}^{2+}] = 0.2 \text{ M}$ and $[\text{Na}^+] = 0.2 \text{ M}$ (sample no. 7), (b) $[\text{Ca}^{2+}] = 0.4 \text{ M}$ and $[\text{Na}^+] = 0.2 \text{ M}$ (sample no. 8), (c) $[\text{Ca}^{2+}] = 0.6 \text{ M}$ and $[\text{Na}^+] = 0.2 \text{ M}$ (sample no. 9), (d) $[\text{Ca}^{2+}] = 0.2 \text{ M}$ and $[\text{Na}^+] = 0.4 \text{ M}$ (sample no. 11), (e) $[\text{Ca}^{2+}] = 0.4 \text{ M}$ and $[\text{Na}^+] = 0.4 \text{ M}$ (sample no. 11), (f) $[\text{Ca}^{2+}] = 0.6 \text{ M}$ and $[\text{Na}^+] = 0.4 \text{ M}$ (sample no. 12), (g) $[\text{Ca}^{2+}] = 0.2 \text{ M}$ and $[\text{Na}^+] = 0.6 \text{ M}$ (sample no. 13), (h) $[\text{Ca}^{2+}] = 0.4 \text{ M}$ and $[\text{Na}^+] = 0.6 \text{ M}$ (sample no. 14), and (i) $[\text{Ca}^{2+}] = 0.6 \text{ M}$ and $[\text{Na}^+] = 0.6 \text{ M}$ (sample no. 15).

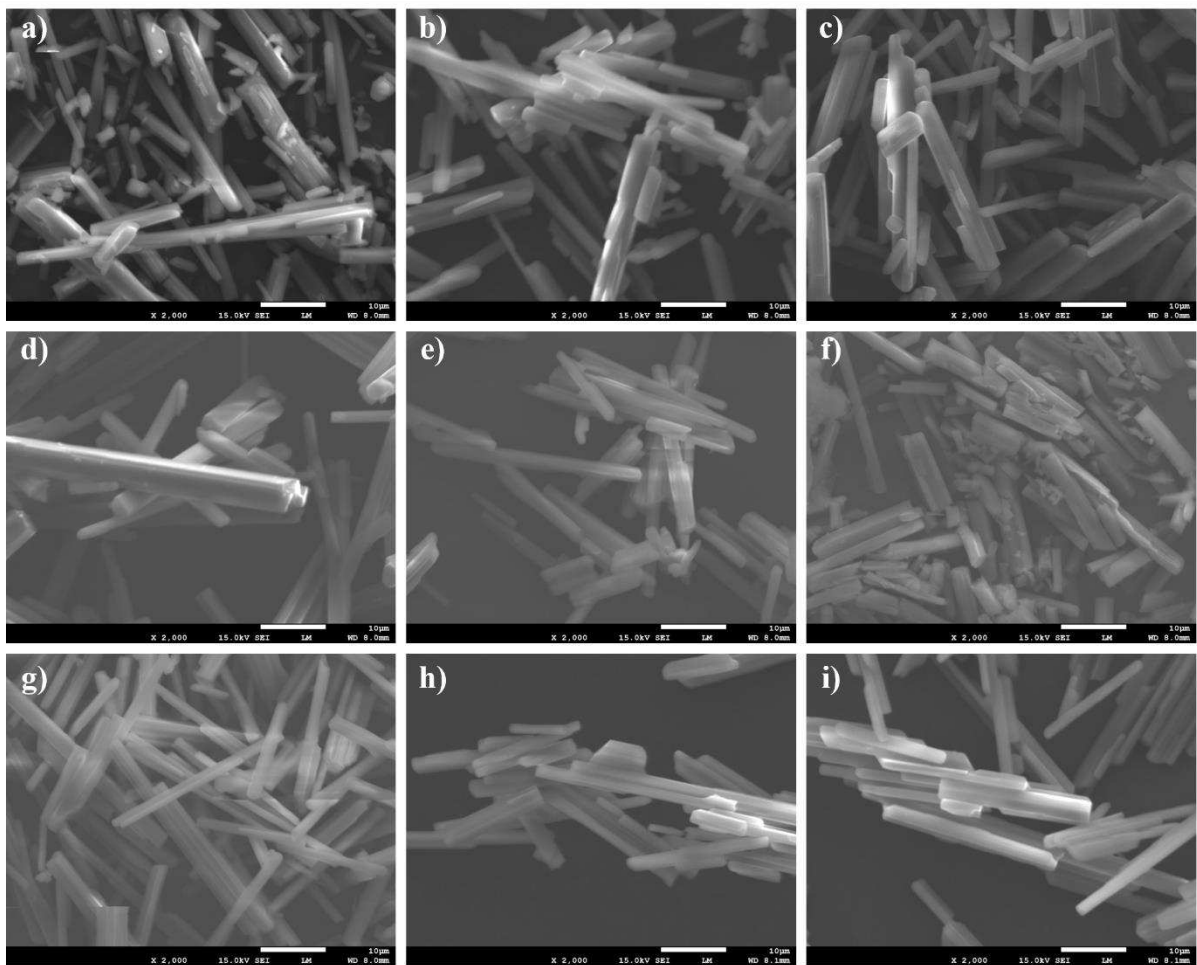


Fig. 8. FE-SEM images of precipitates from system MN. Each images shows crystal shape of precipitate in each sample according to Mg^{2+} and Na^+ concentration. (a) $[Mg^{2+}] = 0.2$ M and $[Na^+] = 0.2$ M (sample no. 16), (b) $[Mg^{2+}] = 0.4$ M and $[Na^+] = 0.2$ M (sample no. 17), (c) $[Mg^{2+}] = 0.6$ M and $[Na^+] = 0.2$ M (sample no. 18), (d) $[Mg^{2+}] = 0.2$ M and $[Na^+] = 0.4$ M (sample no. 19), (e) $[Mg^{2+}] = 0.4$ M and $[Na^+] = 0.4$ M (sample no. 20), (f) $[Mg^{2+}] = 0.6$ M and $[Na^+] = 0.4$ M (sample no. 21), (g) $[Mg^{2+}] = 0.2$ M and $[Na^+] = 0.6$ M (sample no. 22), (h) $[Mg^{2+}] = 0.4$ M and $[Na^+] = 0.6$ M (sample no. 23), and (i) $[Mg^{2+}] = 0.6$ M and $[Na^+] = 0.6$ M (sample no. 24).

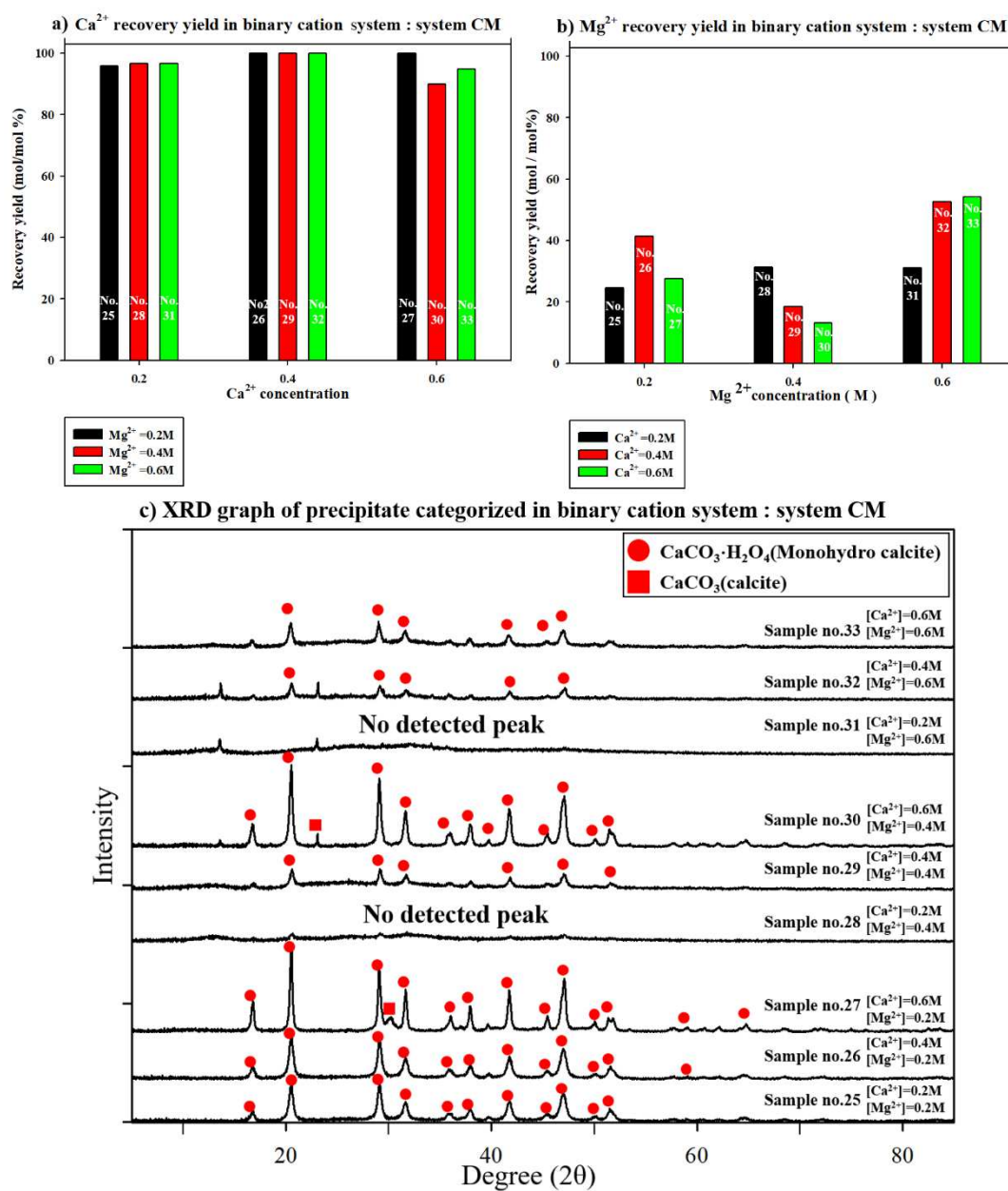


Fig. 9. Cation precipitation trend in system CM. (a) Ca^{2+} recovery yield in system CM with Ca^{2+} and Mg^{2+} concentration (number in the bar is sample number) and (b) Mg^{2+} recovery yield in system CM with Mg^{2+} and Ca^{2+} concentration. (c) XRD graphs of precipitates in system CM.

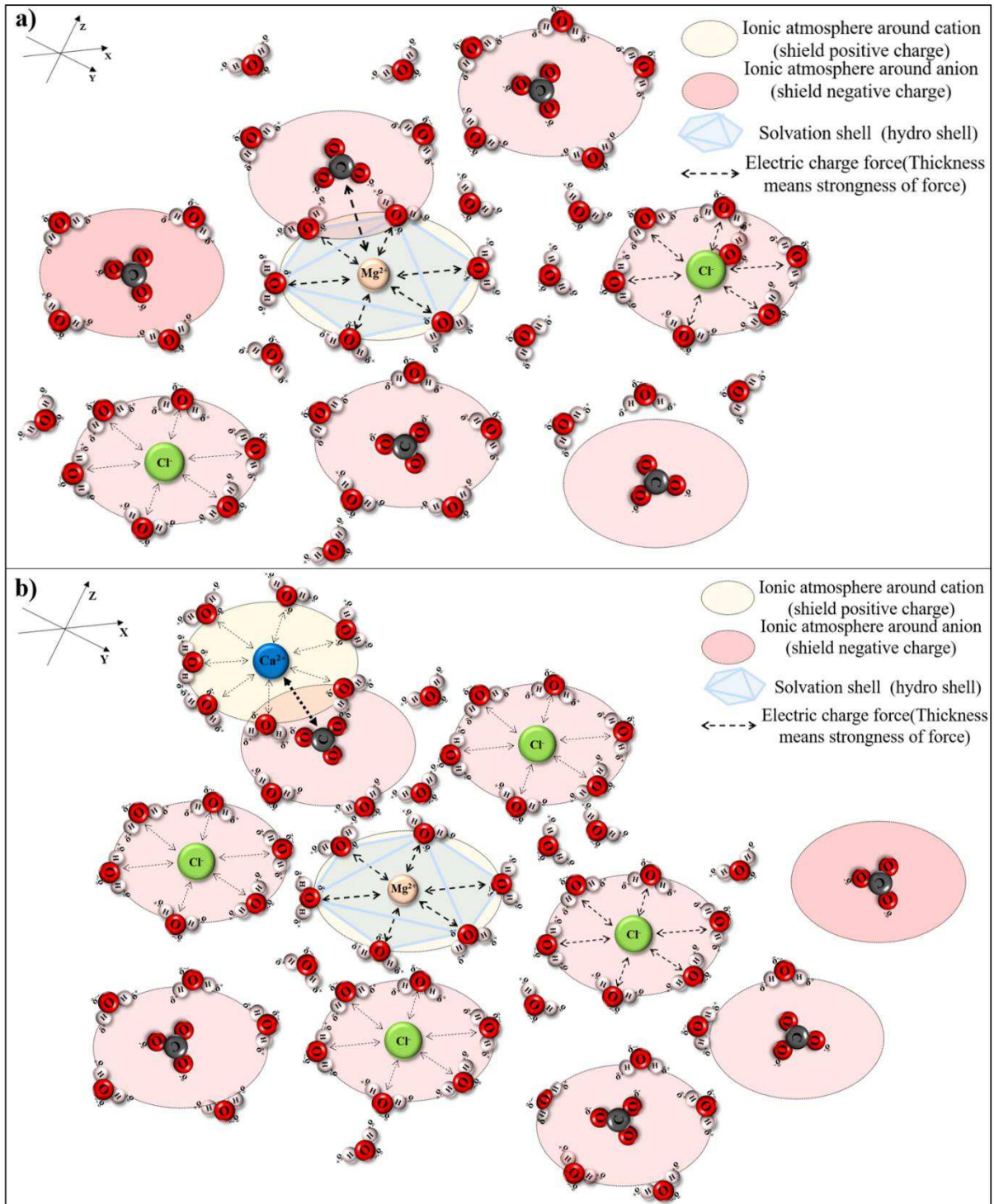


Fig. 10 Driving force of dication recovery decrease. The common ion effect occurs by enhanced ionic strength, which affects carbonation. – a) MgCO_3 formation in system Mg^{2+} , b) CaCO_3 formation and common ion effect (salting-in effect) in system CM

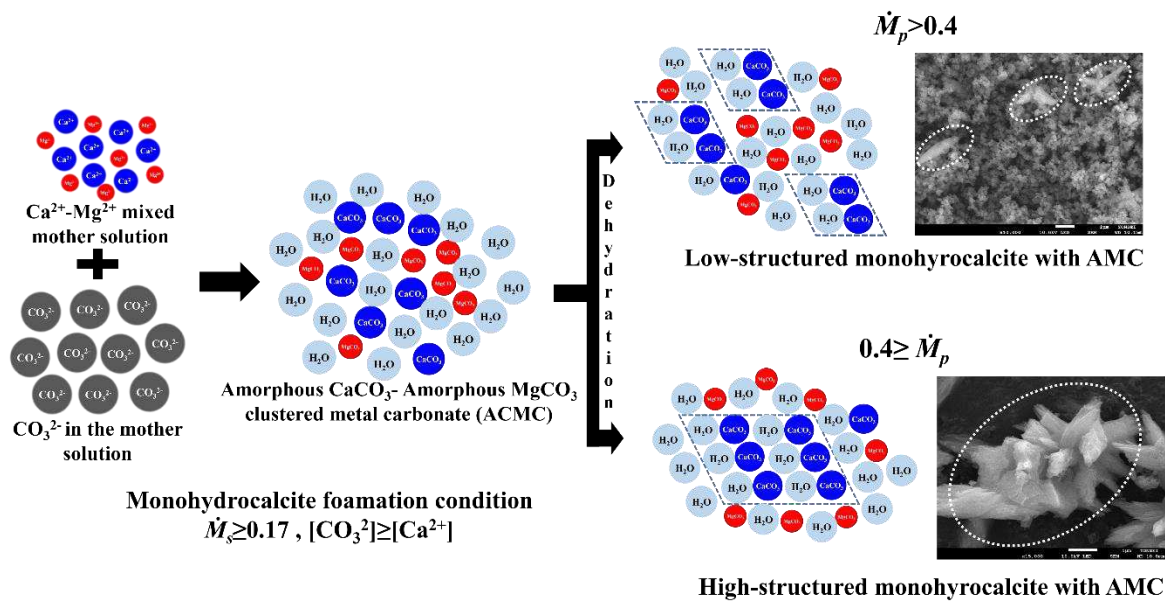


Fig. 11 Monohydrocalcite formation process in Ca–Mg-rich mother solution: In mother solution, Ca^{2+} and Mg^{2+} first formed ACC and AMC and precipitated with a mixed cluster of ACC and AMC, usually called ACMC. After that, ACC dehydrated and monohydrocalcite formed in ACMC [24, 27, 42, 43].

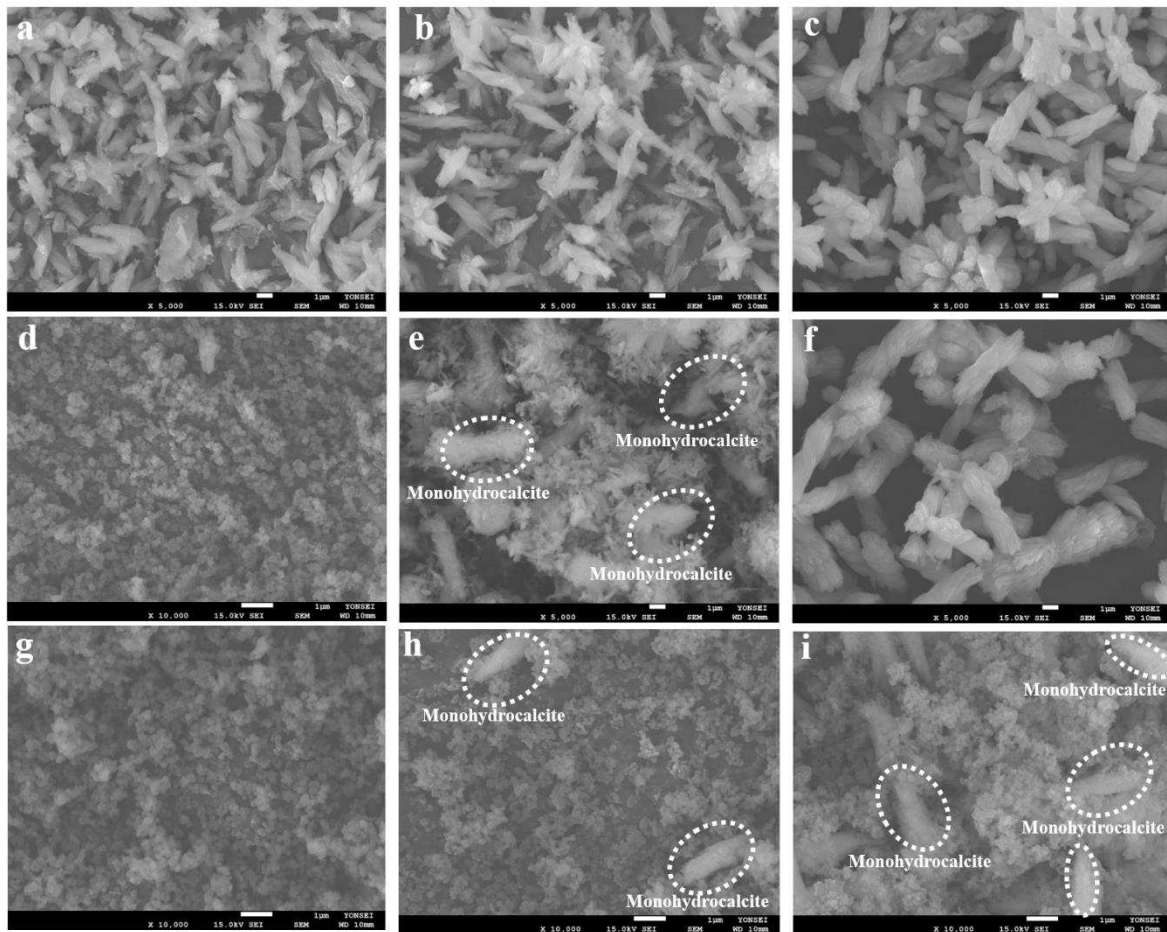


Fig. 12. FE-SEM images of precipitates from system CM. Each image shows crystal shape of precipitate in each sample according to its Ca^{2+} and Mg^{2+} concentration. (Dash-lined circle indicates low structured monohydrocalcite): (a) $[\text{Ca}^{2+}] = 0.2 \text{ M}$ and $[\text{Mg}^{2+}] = 0.2 \text{ M}$ (sample no. 25), (b) $[\text{Ca}^{2+}] = 0.4 \text{ M}$ and $[\text{Mg}^{2+}] = 0.2 \text{ M}$ (sample no. 26), (c) $[\text{Ca}^{2+}] = 0.6 \text{ M}$ and $[\text{Mg}^{2+}] = 0.2 \text{ M}$ (sample no. 27), (d) $[\text{Ca}^{2+}] = 0.2 \text{ M}$ and $[\text{Mg}^{+}] = 0.4 \text{ M}$ (sample no. 28), (e) $[\text{Ca}^{2+}] = 0.4 \text{ M}$ and $[\text{Mg}^{2+}] = 0.4 \text{ M}$ (sample no. 29), (f) $[\text{Ca}^{2+}] = 0.6 \text{ M}$ and $[\text{Mg}^{2+}] = 0.4 \text{ M}$ (sample no. 30), (g) $[\text{Ca}^{2+}] = 0.2 \text{ M}$ and $[\text{Mg}^{2+}] = 0.6 \text{ M}$ (sample no. 31), (h) $[\text{Ca}^{2+}] = 0.4 \text{ M}$ and $[\text{Mg}^{2+}] = 0.6 \text{ M}$ (sample no. 32), (i) $[\text{Ca}^{2+}] = 0.6 \text{ M}$ and $[\text{Mg}^{+}] = 0.6 \text{ M}$ (sample no. 33).

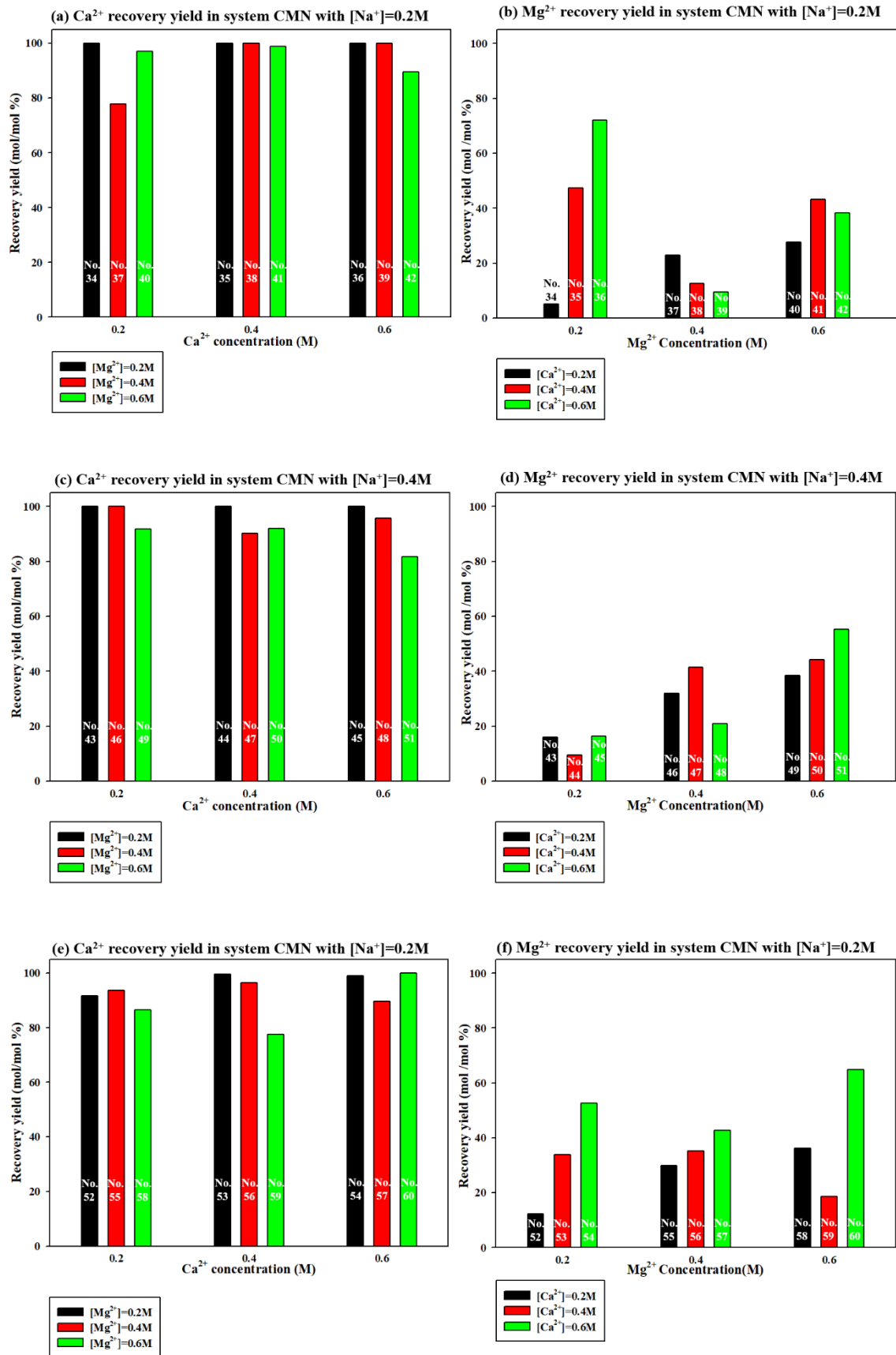
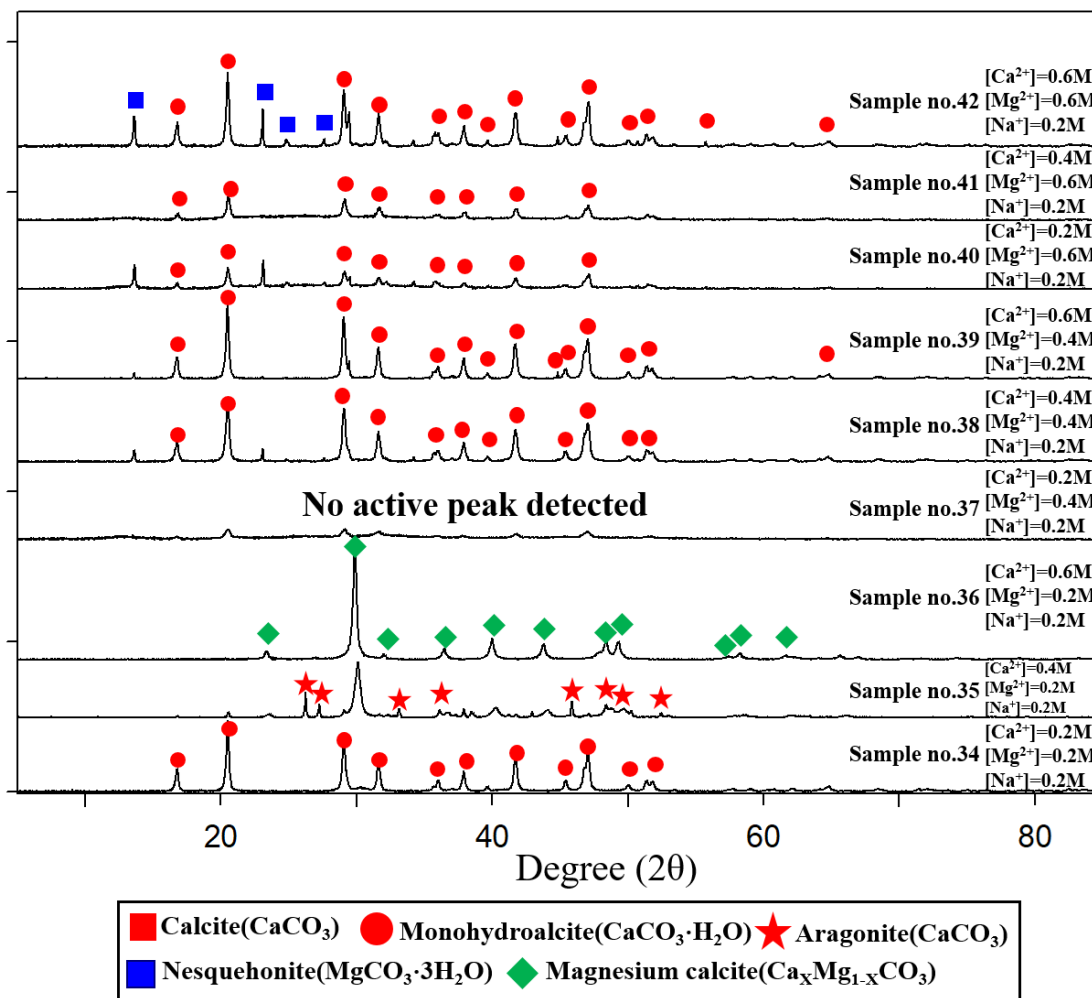


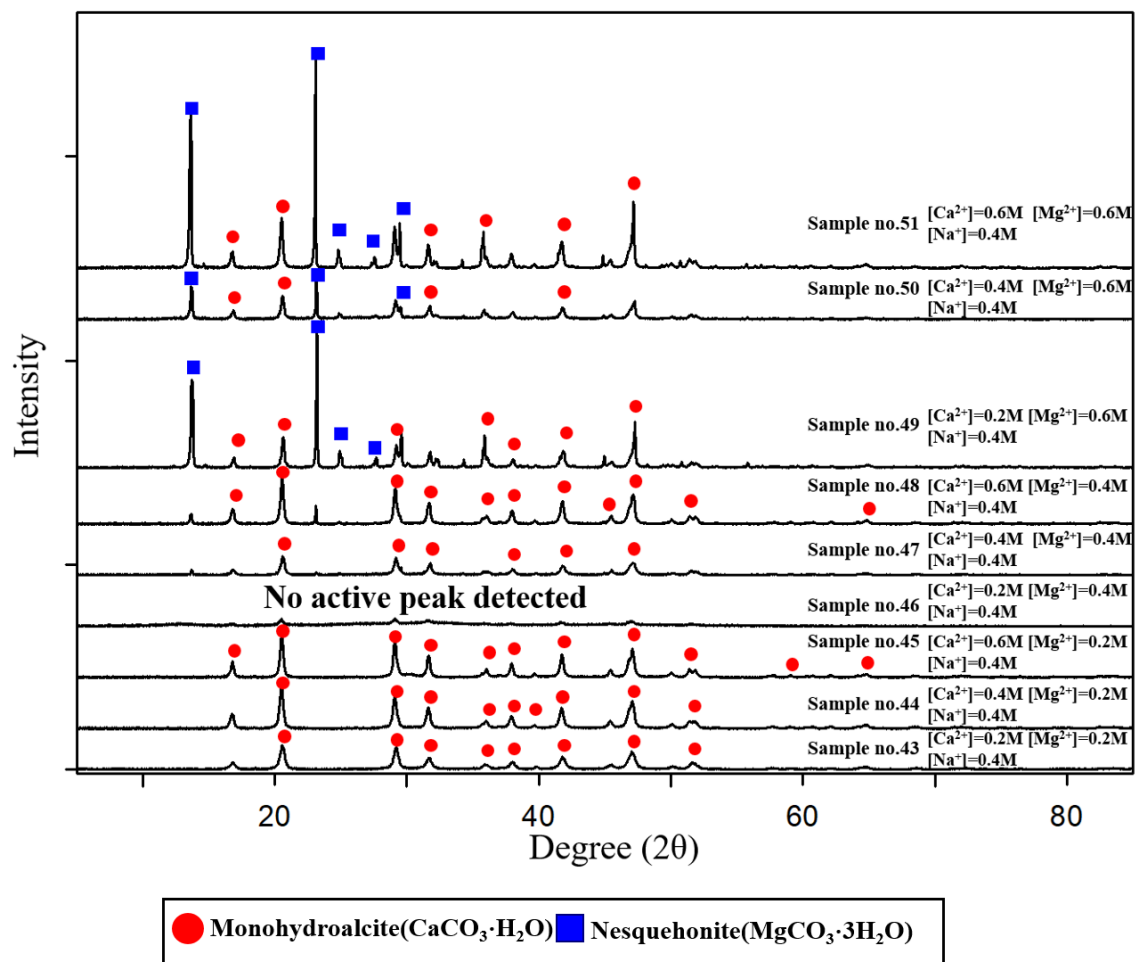
Fig. 13. Cation recovery yield in system CMM according to Na⁺ concentration. (a) Ca²⁺ recovery yield

in system CMN with Ca^{2+} concentration in $[\text{Na}^+] = 0.2 \text{ M}$, (b) Mg^{2+} recovery yield in system CMN with Mg^{2+} concentration in $[\text{Na}^+] = 0.2 \text{ M}$, (c) Ca^{2+} recovery yield in system CMN with Ca^{2+} concentration in $[\text{Na}^+] = 0.4 \text{ M}$, (d) Mg^{2+} recovery yield in system CMN with Mg^{2+} concentration in $[\text{Na}^+] = 0.4 \text{ M}$, (e) Ca^{2+} recovery yield in system CMN with Ca^{2+} concentration in $[\text{Na}^+] = 0.6 \text{ M}$, and (f) Mg^{2+} recovery yield in system CMN with Mg^{2+} concentration in $[\text{Na}^+] = 0.6 \text{ M}$.

(a) XRD graph of system CMN with $[\text{Na}^+]=0.2\text{M}$



(b) XRD graph of system CMN with $[\text{Na}^+] = 0.4\text{M}$



(c) XRD graph of system CMN with $[\text{Na}^+]=0.6\text{M}$

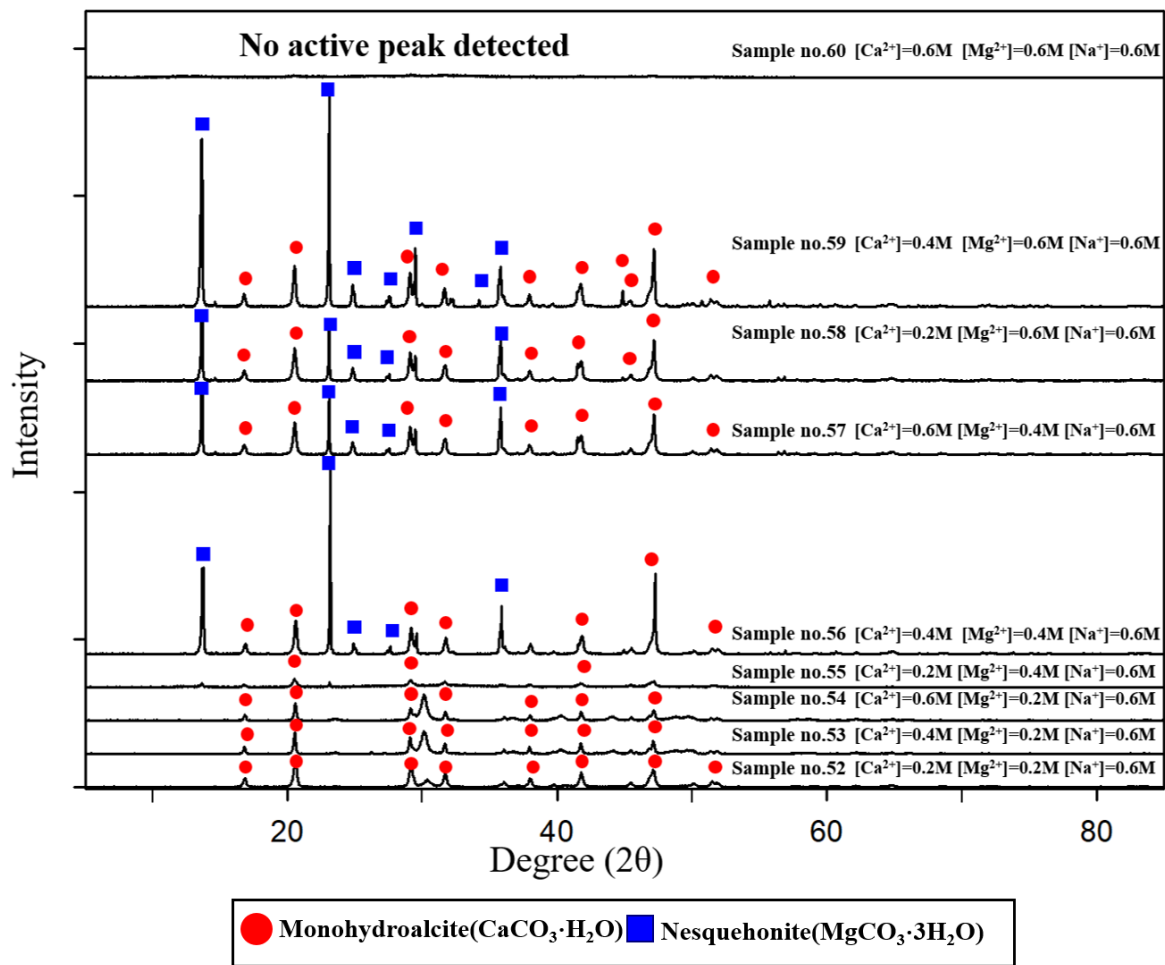


Fig. 14. XRD graphs of system CMN –(a) XRD graphs of system CMN with $[\text{Na}^+] = 0.2\text{M}$, (b) XRD graphs of system CMN with $[\text{Na}^+] = 0.4\text{M}$, (c) XRD graphs of system CMN with $[\text{Na}^+] = 0.6\text{M}$

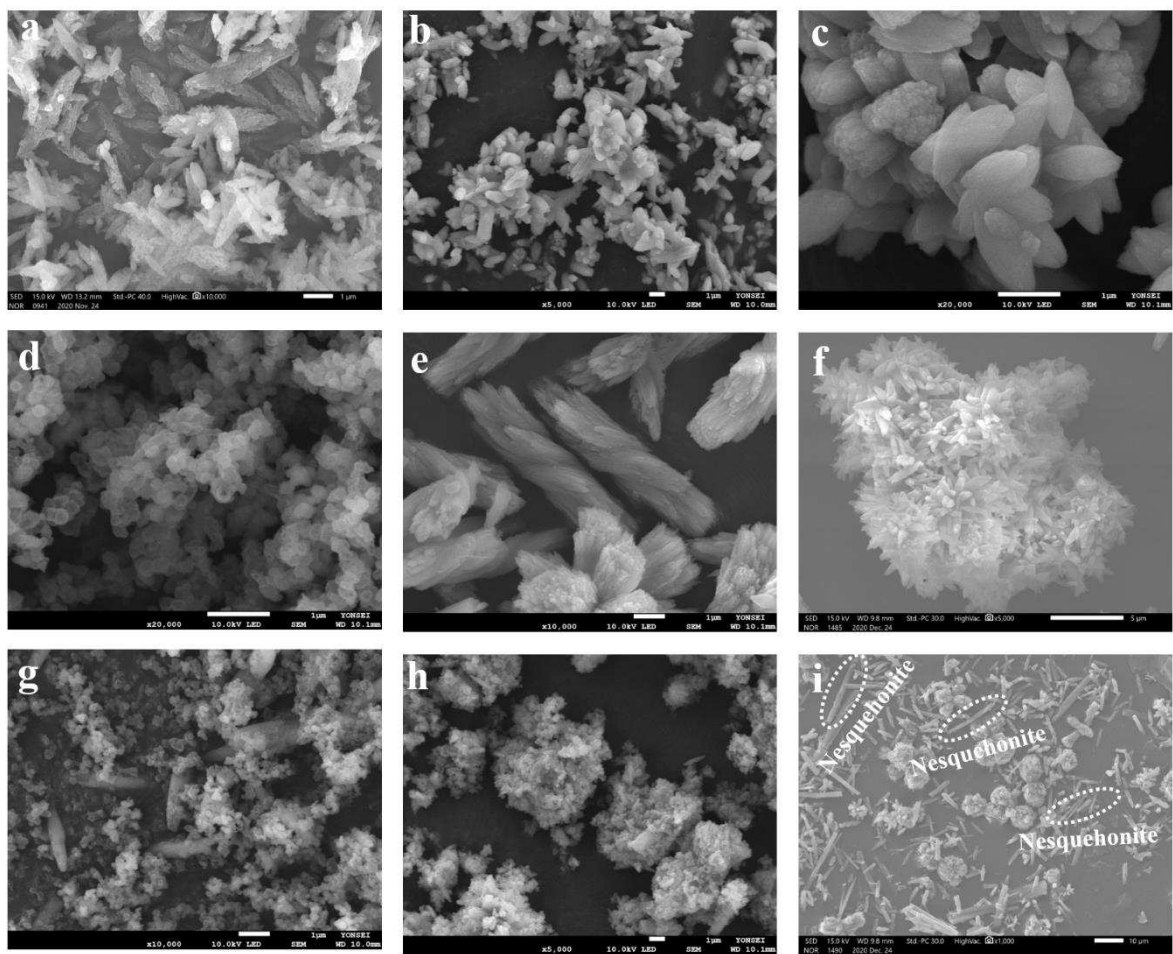


Fig. 15. FE-SEM images of precipitates categorized in ternary cation system CMN with $[\text{Na}^+] = 0.2 \text{ M}$. Each image is from a different precipitate sample: (a) sample 34, (b) sample 35, (c) sample 36, (d) sample 37, (e) sample 38, (f) sample 39, (g) sample 40, (h) sample 41, and (i) sample 42.

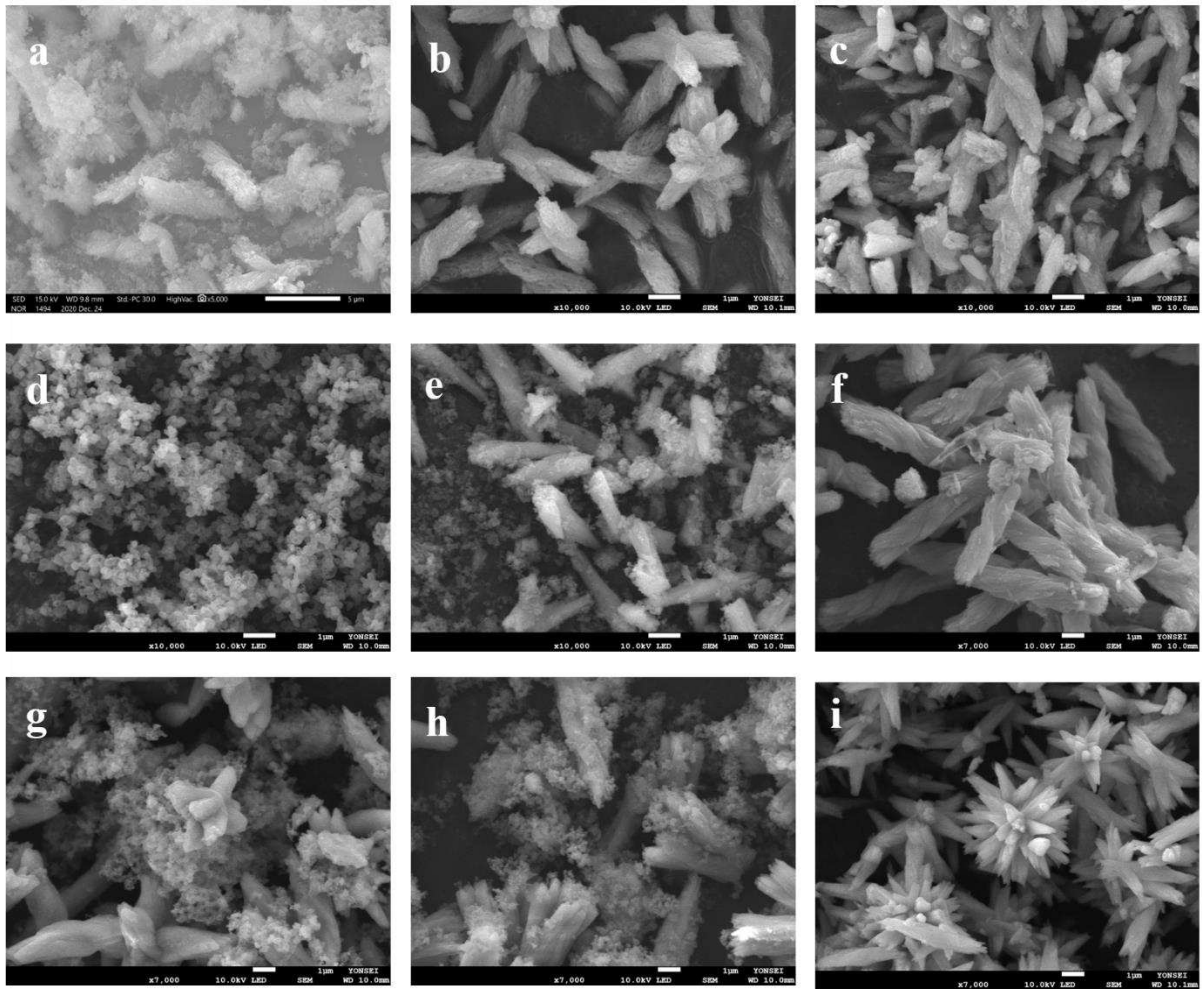


Fig. 16. FE-SEM images of precipitates categorized in ternary cation system CMN with $[\text{Na}^+] = 0.4 \text{ M}$. Each image is from a different precipitate sample: (a) sample 43, (b) sample 44, (c) sample 45, (d) sample 46, (e) sample 47, (f) sample 48, (g) sample 49, (h) sample 50, and (i) sample 51.

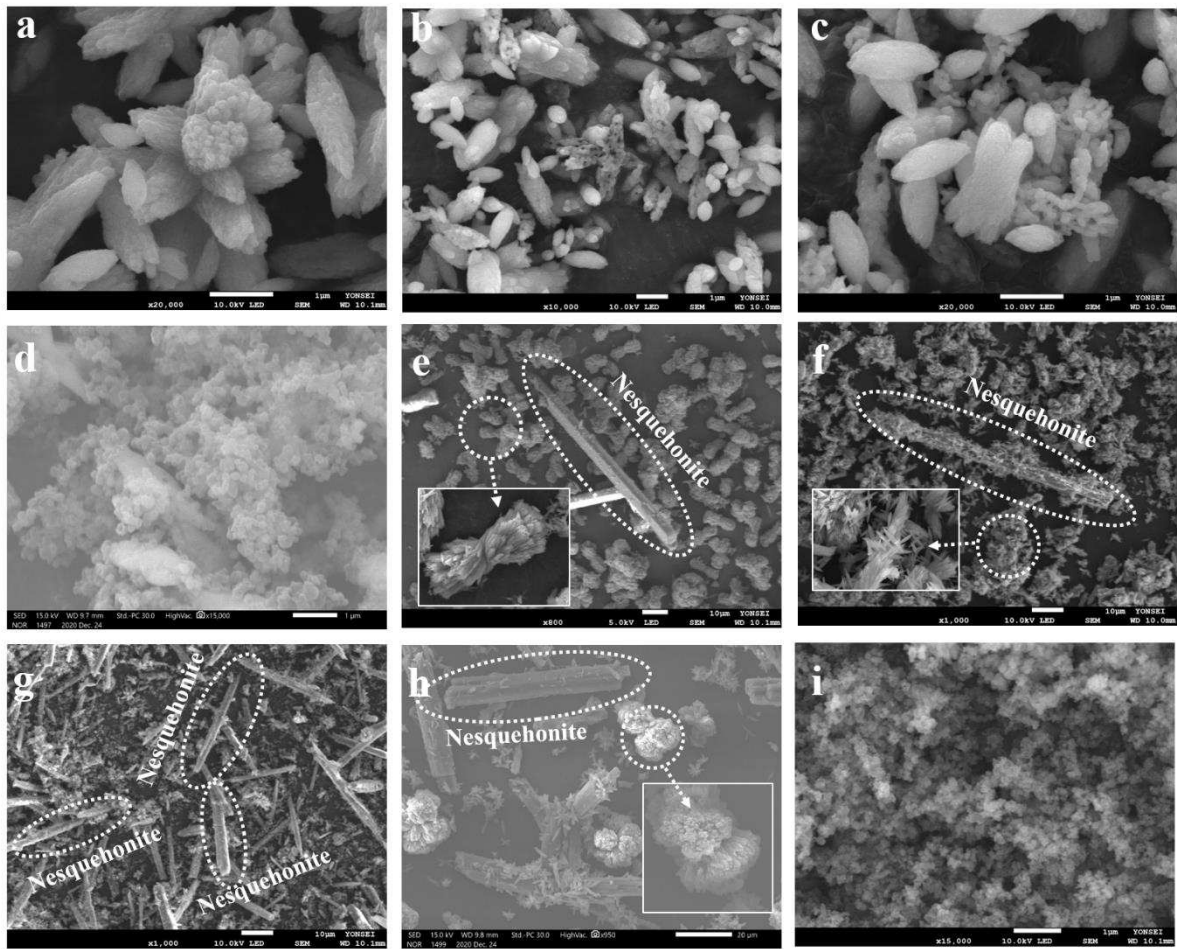


Fig. 17. FE-SEM images of precipitate categorized in ternary cation system CMN with $[\text{Na}^+] = 0.6 \text{ M}$. Each image is from a different precipitate sample: (a) sample 52, (b) sample 53, (c) sample 54, (d) sample 55, (e) sample 56, (f) sample 57, (g) sample 58, (h) sample 59, and (i) sample 60

Table 1. Cation components of each simulated desalination brine samples and stirring conditions

System type	Subcategory of system	Sample number	Cation concentration (mol/L)			
			Ca ²⁺	Mg ²⁺	Na ⁺	
Unary system	System Ca ²⁺	1	0.2			
		2	0.4	-		
		3	0.6			
	System Mg ²⁺	4		0.2	-	
		5	-	0.4		
		6		0.6		
Binary system	System CN (Ca ²⁺ + Na ⁺)	7	0.2			
		8	0.4		0.2	
		9	0.6			
		10	0.2			
		11	0.4	-	0.4	
		12	0.6			
	System MN (Mg ²⁺ + Na ⁺)	13	0.2			
		14	0.4		0.6	
		15	0.6			
		16		0.2		
		17		0.4	0.2	
		18		0.6		
		19		0.2		
		20	-	0.4	0.4	
	System CM (Ca ²⁺ + Mg ²⁺)	21		0.6		
22			0.2			
23			0.4	0.6		
24			0.6			
25		0.2				
26		0.4	0.2			
27		0.6				
Ternary system	System CMN (Ca ²⁺ + Mg ²⁺ + Na ⁺)	28	0.2			
		29	0.4	0.4	0.0	
		30	0.6			
		31	0.2			
		32	0.4	0.6		
		33	0.6			
		34	0.2			
	System CMN (Ca ²⁺ + Mg ²⁺ + Na ⁺)	35	0.4	0.2		
		36	0.6			
		37	0.2			
		38	0.4	0.4	0.2	
		39	0.6			
		40	0.2			
		41	0.4	0.6		
42	0.6					
Ternary system	System CMN (Ca ²⁺ + Mg ²⁺ + Na ⁺)	43	0.2			
		44	0.4	0.2		
		45	0.6			
		46	0.2			
		47	0.4	0.4	0.4	
		48	0.6			
		49	0.2			
	50	0.4	0.6			
	51	0.6				
	Ternary system	System CMN (Ca ²⁺ + Mg ²⁺ + Na ⁺)	52	0.2		
			53	0.4	0.2	
			54	0.6		
			55	0.2		
			56	0.4	0.4	0.6
57			0.6			
58			0.2			
59			0.4	0.6		
60			0.6			

Table 2. Cation recovery yield in accordance with cation concentration in each simulated brine sample

	Sample no.	Cation concentration (M)	Cation recovery yield (mol/mol %)	Crystal phase composition (%)	
				Calcite (CaCO ₃)	Vaterite (CaCO ₃)
Result of system Ca²⁺	1	0.2	92.62	22.5	77.5
	2	0.4	98.12	13.8	86.2
	3	0.6	99.99	LOQ	99.9
Result of system Mg²⁺				Nesquenonite (MgCO ₃ ·3H ₂ O)	
	4	0.2	47.05	99.99	
	5	0.4	62.43	99.99	
	6	0.6	82.76	99.99	

LOQ: Limit of quantitation

Table 3. Results of EDS analysis for precipitates

Sample no.	Element (at.%)			O/metal ratio
	C	O	Ca	O/Ca
1	60.77	33.86	5.37	6.30
2	35.90	53.87	10.24	5.26
3	33.71	52.64	13.64	3.86
	C	O	Mg	O/Mg
4	22.27	67.95	9.78	6.95
5	22.08	68.64	9.28	7.39
6	19.26	68.44	12.31	5.56

Table 4. Cation recovery yield in accordance with cation concentration in each simulated brine sample

System type	Sample no.	Cation concentration (M)		Cation recovery yield (mol/mol %)		Crystal phase composition (%)	
		Ca ²⁺	Na ⁺	Ca ²⁺	Na ⁺	Calcite (CaCO ₃)	Vaterite (CaCO ₃)
system CN	7	0.2		99.99	0.82	LOQ	96.1
	8	0.4	0.2	99.99	1.96	LOQ	96.9
	9	0.6		99.99	3.29	LOQ	97.4
	10	0.2		92.67	3.61	LOQ	98.1
	11	0.4	0.4	98.34	4.76	LOQ	99.2
	12	0.6		99.99	4.32	LOQ	99.9
	13	0.2		97.87	1.01	LOQ	99.1
	14	0.4	0.6	99.99	1.03	LOQ	99.9
	15	0.6		99.99	1.55	LOQ	99.9
system MN		Mg ²⁺	Na ⁺	Mg ²⁺	Na ⁺	Nesquenonite (MgCO ₃ ·3H ₂ O)	
	16	0.2		49.97	LOQ	99.9	
	17	0.4	0.2	63.14	LOQ	99.9	
	18	0.6		90.33	LOQ	99.9	
	19	0.2		56.02	LOQ	99.9	
	20	0.4	0.4	78.43	LOQ	99.9	
	21	0.6		89.80	LOQ	99.9	
	22	0.2		52.56	LOQ	99.9	
	23	0.4	0.6	78.38	LOQ	99.9	
24	0.6		87.19	LOQ	99.9		
system CM		Ca ²⁺	Mg ²⁺	Ca ²⁺	Mg ²⁺	Monohydro calcite (CaCO ₃ ·H ₂ O)	Calcite (CaCO ₃)
	25	0.2		95.96	24.55	99.9	LOQ
	26	0.4	0.2M	99.99	41.34	99.9	LOQ
	27	0.6		99.99	27.50	91.1	8.9
	28	0.2		96.68	31.36	LOQ	LOQ
	29	0.4	0.4M	99.99	46.09	99.9	LOQ
	30	0.6		90.95	13.09	90.4	9.6
	31	0.2		96.72	31.10	LOQ	LOQ
	32	0.4	0.6M	99.99	52.75	99.9	LOQ
33	0.6		94.90	54.32	99.9	LOQ	

*LOQ: Limit of quantitation

Table 5. Results of EDS analysis for precipitate of binary cation system

System type	Sample no.	Element (at.%)				\dot{h} (O/Meta) ratio
		C	O	Na	Ca	O/Ca
Result of system CN	7	37.67	53.21	LOQ	9.11	5.84
	8	43.15	46.81	LOQ	10.04	4.66
	9	33.59	51.12	LOQ	15.29	3.34
	10	37.39	54.61	LOQ	8.00	6.83
	11	40.21	50.93	LOQ	8.86	5.75
	12	38.12	51.28	LOQ	10.60	4.84
	13	39.13	52.13	LOQ	8.74	5.96
	14	41.24	49.77	LOQ	8.99	5.54
	15	34.50	54.24	LOQ	11.26	4.82
Result of system MN		C	O	Na	Mg	O/Mg
	16	25.75	66.52	LOQ	7.73	8.61
	17	25.92	65.91	LOQ	8.17	8.07
	18	24.17	67.65	LOQ	8.17	8.28
	19	18.23	71.19	LOQ	10.58	6.73
	20	31.81	61.71	LOQ	6.48	9.52
	21	21.72	67.96	LOQ	10.32	6.59
	22	23.94	66.79	LOQ	9.27	6.59
23	21.59	68.87	LOQ	9.54	7.22	
24	23.35	67.00	LOQ	9.65	6.94	
Result of system CM		C	O	Ca	Mg	O/(Mg+Ca)
	25	40.8	51.67	5.42	2.1	6.87
	26	41.21	50.84	6.03	1.92	6.39
	27	35.64	55.48	8.32	0.56	6.25
	28	62.62	34.07	1.67	1.65	10.26
	29	60.68	35.65	2.99	0.67	9.74
	30	29.2	61.35	9.1	0.57	6.33
	31	78.13	20.55	0.59	0.73	15.57
32	83.18	15.67	0.57	0.58	13.63	
33	48.73	45.46	3.4	2.41	7.82	

*LOQ: Limit of quantitation

Table 6. Cation composition of precipitate from simulated desalination brine of system CM

Sample number	Solution		Precipitate	
	M_s (mol/mol)	Ca ²⁺ concentration (mmol/g)	Mg ²⁺ concentration (mmol/g)	M_p (mol/mol)
25	1	7.19	1.84	0.26
26	0.5	6.84	1.42	0.21
27	0.33	8.23	0.76	0.09
28	2	4.78	3.10	0.66
29	1	4.34	2.00	0.47
30	0.67	8.23	0.76	0.10
31	3	3.94	3.81	0.98
32	1.5	4.33	3.44	0.80
33	1	4.23	2.42	0.58

$M = [\text{Mg}^{2+}]/[\text{Ca}^{2+}]$ (unit: mol/mol. M_s : M of simulated desalination brine, M_p : M of precipitate)

mmol/g: mmol of cation in g of precipitation

Table 7. Cation recovery yield for precipitate of system CMN with $[\text{Na}^+] = 0.2 \text{ M}$ in accordance with cation concentration in each simulated brine with sample

System type	Sample No.	Cation concentration (M)			Cation recovery yield (mol/mol%)			Crystal phase composition (%)		
		Ca^{2+}	Mg^{2+}	Na^+	Ca^{2+}	Mg^{2+}	Na^+	Monohydro calcite	Magnesian calcite	Nesquehonite
Result of system CMN with $[\text{Na}^+] = 0.2 \text{ M}$	34	0.2			99.99	5.19	0.62	98.6	LOQ	LOQ
	35	0.4	0.2		99.99	47.32	1.59	99.9	LOQ	LOQ
	36	0.6			99.99	71.98	2.22	LOQ	99.9	LOQ
	37	0.2			77.92	22.93	0.99	LOQ	LOQ	LOQ
	38	0.4	0.4	0.2	99.99	12.66	0.60	99.5	LOQ	LOQ
	39	0.6			99.99	9.42	0.63	93.3	LOQ	LOQ
	40	0.2			97.08	27.54	1.34	99.9	LOQ	LOQ
	41	0.4	0.6		98.84	43.27	1.78	99.9	LOQ	LOQ
	42	0.6			89.59	38.22	0.52	77.4	LOQ	21.4
Result of system CMN with $[\text{Na}^+] = 0.4 \text{ M}$	43	0.2			99.99	15.96	0.75	93.2	LOQ	LOQ
	44	0.4	0.2		99.99	9.38	0.91	97.9	2.1	LOQ
	45	0.6			99.99	16.45	1.85	99.9	LOQ	LOQ
	46	0.2			99.99	32.00	0.81	LOQ	LOQ	LOQ
	47	0.4	0.4	0.4	90.15	41.47	3.18	94.8	LOQ	LOQ
	48	0.6			95.65	20.96	1.60	98.8	LOQ	LOQ
	49	0.2			91.76	38.51	1.20	66.7	LOQ	34.3
	50	0.4	0.6		92.00	44.29	2.99	62.0	LOQ	38.0%
	51	0.6			81.67	55.28	3.44	36.6	LOQ	63.4%
Result of system CMN with $[\text{Na}^+] = 0.6 \text{ M}$	52	0.2			91.67	12.25	0.44	99.9	LOQ	LOQ
	53	0.4	0.2		99.61	33.83	1.40	99.9	LOQ	LOQ
	54	0.6			99.01	52.71	2.17	99.9	LOQ	LOQ
	55	0.2			93.61	29.82	0.91	99.9	LOQ	LOQ
	56	0.4	0.4	0.6	96.46	35.15	0.58	39.0	LOQ	61.0
	57	0.6			89.68	42.82	2.10	53.2	LOQ	46.8
	58	0.2			86.55	36.21	1.35	71.0	LOQ	29.0
	59	0.4	0.6		77.44	42.66	0.95	33.5	LOQ	66.5
	60	0.6			99.99	64.80	4.12	LOQ	LOQ	LOQ

*LOQ: Limit of quantitation

Table 8. Cation composition of precipitate from simulated desalination brine of system CNM

System type	Sample No.	Solution		Precipitate	
		M_s (mol/mol)	Ca ²⁺ concentration (mmol/g)	Mg ²⁺ concentration (mmol/g)	M_p (mol/mol)
Result of system CMN with [Na ⁺] = 0.2 M	34	1	8.92	0.46	0.05
	35	0.5	8.22	1.95	0.24
	36	0.33	8.05	1.94	0.24
	37	2	5.02	2.96	0.59
	38	1	7.68	0.97	0.13
	39	0.67	8.06	0.51	0.06
	40	3	4.00	3.41	0.85
	41	1.5	3.45	2.27	0.66
	42	1	5.83	2.49	0.43
	Result of system CMN with [Na ⁺] = 0.4 M	43	1	7.85	1.25
44		0.5	8.43	0.40	0.05
45		0.33	8.43	0.46	0.05
46		2	7.78	4.99	0.64
47		1	4.96	2.29	0.46
48		0.67	7.32	1.07	0.15
49		3	3.39	4.28	1.26
50		1.5	4.03	2.91	0.72
51		1	4.39	2.98	0.67
Result of system CMN with [Na ⁺] = 0.6 M		52	1	7.88	1.05
	53	0.5	8.08	1.37	0.17
	54	0.33	8.09	1.44	0.18
	55	2	4.73	3.02	0.64
	56	1	6.02	2.20	0.37
	57	0.67	5.71	1.82	0.32
	58	3	3.30	4.14	1.26
	59	1.5	3.66	3.03	0.83
	60	1	4.89	3.18	0.65

$M = [Mg^{2+}] / [Ca^{2+}]$ (unit: mol/mol. M : M of simulated desalination brine, M_p : M of precipitate)

mmol/g: mmol of cation in g of precipitation

Table 9. Results of EDS analysis for precipitate from simulated desalination brine categorized in system CMN

System type	Sample no.	Element (at.%)					O/metal ratio
		C	O	Ca	Mg	Na	(<i>h</i> _{Di}) O/Metal
system CMN with [Na ⁺] = 0.2 M	34	57.16	38.03	4.52	0.29	LOQ	7.91
	35	36.92	53.68	6.72	2.38	0.3	5.9
	36	32.75	55.44	9.04	2.36	0.41	4.86
	37	37.25	55.14	7.61	0	LOQ	7.25
	38	37.51	54.88	7.24	0.37	LOQ	7.21
	39	29.02	60.61	9.97	0.39	LOQ	5.85
	40	66.46	30.12	1.57	1.85	LOQ	8.81
	41	43.36	48.2	4.84	3.49	0.11	5.79
	42	27.84	58.03	13.05	1.08	0	4.11
	system CMN with [Na ⁺] = 0.4 M	43	41.95	51.24	5.65	1.05	0.12
44		29.12	59.62	10.6	0.51	0.14	5.37
45		38.88	50.35	10.31	0.31	0.14	4.74
46		60.69	36.06	1.55	1.63	0.08	11.34
47		40.43	51.05	6.28	2.16	0.08	6.05
48		34.93	54.92	9.13	0.88	0.13	5.49
49		30.39	56.19	4.33	8.77	0.31	4.29
50		29.52	54.79	12.07	3.36	0.27	3.55
51		37.33	49.63	9.88	3.16	LOQ	3.81
system CMN with [Na ⁺] = 0.6 M	52	31.3	59.34	8.42	0.79	0.15	6.44
	53	35.24	54.99	8.14	1.33	0.29	5.81
	54	24.41	60.17	13.45	1.66	0.3	3.98
	55	67.14	29.7	1.61	1.43	0.12	9.55
	56	36.28	40.51	21.9	1.15	0.16	4.39
	57	27.67	59.23	12.43	0.53	0.15	3.33
	58	30.57	57.26	4.96	7.01	0.2	4.78
	59	21.64	64.97	11.75	1.55	0.08	4.88
	60	66.3	30.37	1.68	1.54	0.1	9.43